Doctoral Thesis

Computer-aided Diagnosis
for Female Infertility

by

Kentaro Mori

March 2021

Graduate School of Simulation Studies
University of Hyogo

To my mother and brother
for helping me build the foundations in my life and allowing me to accomplish my
studies.

Abstract

The frequency of infertility treatment is increasing, but the success rate of such treatment is not increasing. A treatment method called assisted reproductive technology (ART) has a higher success rate than conventional fertility treatment. However, the success rate remains low. This study analyzed uterine features of patients with infertility, and developed a medical diagnosis support system for female infertility, to improve the success rate of treatment.

First, features of uterine movements were analyzed by using Cine MRI images. The uterus has movements called uterine peristalsis that assist in the transport of sperm. The direction and frequency of uterine peristalsis change during the phase of each menstrual cycle. However, uterine movements in patients with infertility have not been analyzed in detail. Therefore, the current study analyzed detailed features of uterine movements in infertile patients. This research found six fundamental uterine movements, of which two movements affected infertility. Furthermore, a simulation in this study found that uterine peristalsis had a constant propagation velocity of 0.68 mm/s. Using this simulation velocity feature, a prediction system for uterine movement types was developed by Cine MRI images. This system was composed of a convolutional neural network (CNN). An evaluation experiment showed that the system had a 71% prediction accuracy for sagittal plane images. A system without velocity information had a 64% prediction accuracy for sagittal plane images. These results demonstrated that velocity information was important for uterine movement analysis.

Second, a prediction system for pregnancy outcomes was developed using ultrasonic images and the constant velocity feature. In infertility treatment, it is typical to evaluate the endometrial shape. The CNN system developed in the current study predicted pregnancy outcome by velocity information. Experiments compared the velocity-based and shape-based systems. The shape-based systems predict the optimal uterine features for pregnancy success based on endometrial shape. In this study, two shape-based systems were developed. One used a local binary pattern (LBP), and the other used a CNN. The current findings revealed that the velocity-based system provided similar accuracy to the shape-based systems. However, the output of the velocity-based system, the area under curve (AUC) for the receiver operating characteristic (ROC) curve, provided a higher value than the shape-based systems. The AUC values of the LBP shape-based, CNN shape-based, and velocity-based systems were 0.62, 0.65, and 0.72, respectively. These results showed that the analysis of the velocity of uterine movements was effective for pregnancy outcome prediction. Previous clinical evaluation did not target the uterine movement but only the endometrial shape. Therefore, this study has revealed a new

treatment approach for infertility.

Contents

Chapter 1
Introduction

Infertility is a disorder of the reproductive system. One definition of infertility is the failure to achieve clinical pregnancy after 12 months or more of regular unprotected sexual intercourse [1]. There are two main treatments for infertility: conventional fertility treatment and assisted reproductive technology (ART). Conventional fertility treatment includes timed intercourse and artificial insemination (AIH) using semen. Timed intercourse treatment determines the days with the highest pregnancy rates, by predicting ovulation days based on basal body temperature, ultrasound examination, and hormone measurements. AIH involves inserting artificially extracted semen into the uterus. Conventional fertility treatment is performed as a first step of infertility treatment. When a patient does not get pregnant by conventional treatment, ART is performed as the next treatment step. ART includes in-vitro fertilization (IVF) and may involve intra-cytoplasmic sperm injection (ICSI). In IVF, eggs are fertilized artificially by adding extracted semen or sperm samples to extracted eggs. The fertilized eggs are cultured in the laboratory, and then it returns to the body. In ICSI, egg is fertilized artificially by injecting isolated sperm into an extracted egg. The fertilized eggs are cultured in the laboratory, and then it returns to the body. Figure 1-1 shows the annual frequency of patient treatment and pregnancy rates for ART in Japan [2]. Compared 1990 with 2015, the annual number of ART patients has increased more than 10 times, but the pregnancy rate has remained constant (Figure 1-1). The pregnancy rate in 2017 was 17.7%. Although the pregnancy rate from ART is typically higher than conventional fertility treatment, this rate remains low. Table 1-1 shows the success rate of ART for patients of different ages in the U.S. [3]. The success rate declines with increasing patient age, and pregnancy cannot be guaranteed by a single treatment at these success rates. In general, infertility treatment is repeated until a patient gets pregnant or declines further treatment. Some of the problems of ART include the high cost and physical burden of the treatment, and these problems increase by repeating the treatment. Therefore, improvement of the pregnancy
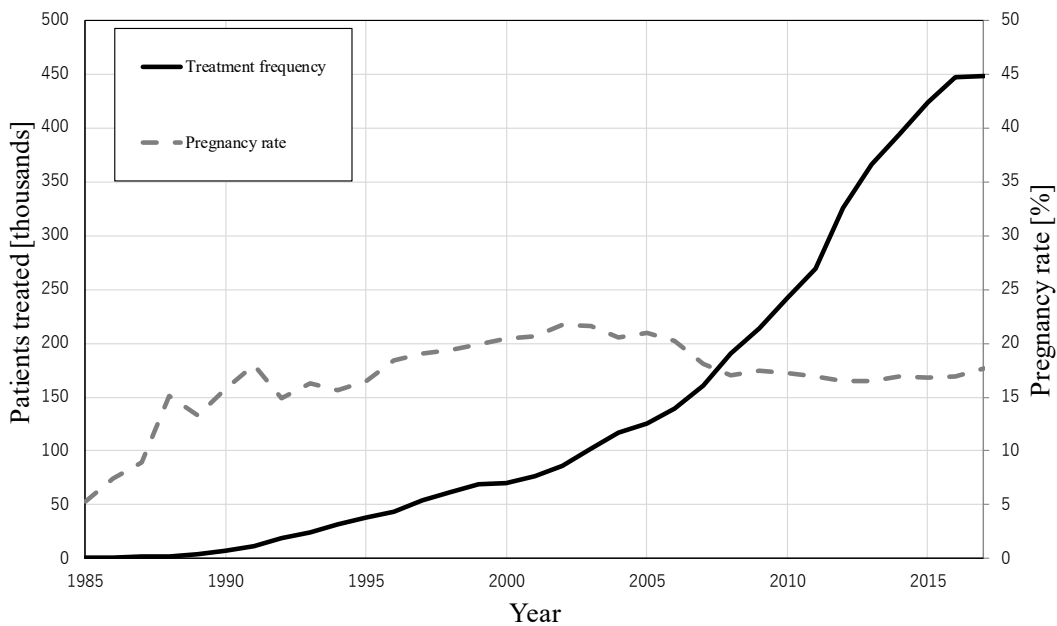
Figure 1-1 Annual infertility treatment frequency and pregnancy rate in Japan.

Table 1-1 Assisted reproduction technology success rates for patient ages.

Patient age (years)	Success rate
< 35	51.6%
35–37	37.5%
38–40	23.5%
41–42	11.8%
≥ 43	3.4%

rate is very important for ART.

ART has four treatment steps: ovulation, sperm retrieval, fertilization, and embryo transfer. In the ovulation step, eggs for fertilization are extracted by carefully inserting a needle into the vagina then ovarian follicle, then withdrawing follicular fluid containing the egg. In the sperm retrieval step, sperm for fertilization are generally extracted from semen samples. Sometimes, sperm is extracted from testis samples by operation if a male patient has azoospermia. In the fertilization step, collected eggs and sperm are combined and fertilized eggs cultured and examined. There are two main methods of fertilization. The IVF method coincubates collected sperm samples and eggs, and the ICSI method involves direct injection of sperm into the egg. In the embryo transfer step, the fertilized egg/embryo is transferred to the uterus. Pregnancy is initiated when the fertilized egg implants in the endometrium. Support systems in the ovulation and fertilization steps using image processing technology have been reported [4 and 5].

Because embryo transfer is a final requirement for ART, the timing of embryo transfer is one of the most important steps in ART. However, this step is the most difficult because there is little artificial intervention possible to optimize implantation after the transfer procedure.

The uterus has movements called uterine peristalsis that assist in the transport of semen. The direction and frequency of peristaltic movements change during each menstrual cycle [6, 7, 8, and 9]. The upward movement (corpus to fundus) occurs in the ovulation phase, and downward movement (fundus to corpus) occurs in the menstrual phase, whereas there are no movements in the luteal phase. However, random and mixed movements occur in all phases of the cycle in infertile patients. To date, these random and mixed movements have not been thoroughly analyzed. Therefore, it is not known which movement has a negative effect on the initiation of pregnancy. Peristaltic movements during the luteal phase strongly affect the embryo transfer procedure. Therefore, analysis of uterine movements may reveal a uterine-derived mechanism of infertility and lead to improvement in successful implantation rates.

In the embryo transfer step, a physician decides the timing of embryo transfer by analyzing endometrial shape using B-mode ultrasonic images. Endometrial shape displayed by ultrasonic imaging changes during the menstrual cycle [10, 11, and 12]. The physician evaluates images of the endometrial shape to determine the menstrual cycle and predict the most effective time for embryo transfer. However, the treatment may fail even if the physician determines a good endometrial condition, and the treatment may succeed even if the physician determines a bad endometrial condition. It is difficult to correctly evaluate a menstrual cycle from endometrial shape. We proposed that the pregnancy outcomes can be predicted correctly by analyzing uterine movement. This method was based on the known changes to the direction and frequency of peristaltic waves throughout each menstrual cycle. A generic changing theory of uterine movement was previously established. However, random and mixed movements in patients with infertility have not been analyzed to date. Investigation of uterine movements in infertile patients may identify features leading to pregnancy failure or success. The frequency of uterine peristalsis is approximately one every few minutes, so it is difficult to analyze uterine movement by visual observation of ultrasonic images. Uterine movement is typically observed using Cine MRI images. During examination, it is difficult to analyze this movement by direct observation because the physician observes images in real time using an ultrasonic device. If these challenges in measuring uterine movements can be solved, we propose that pregnancy outcomes may be predicted from the analysis of uterine movements. Such analysis may lead to the development of a new diagnostic support system to improve the success rate of infertility treatment.

In this study, we aimed to develop a medical diagnosis support system for female infertility based on medical image analysis. This system was composed of a convolutional neural network (CNN), a class of deep neural networks that is composed of a convolution and pooling layer. The CNN has been widely used in image analysis fields, providing high performance analysis in the AlexNet [13], VGGNet [14], and Residual Networks (ResNet) [15]. The CNN has also provided high recognition accuracy in medical image analysis fields, such as lung pattern classification [16], ultrasound detection of breast lesions [17], blood cell image classification by combining a CNN and recursive neural network [18], and feature extraction of tumor images [19].

This thesis is composed of four chapters. **Chapter 1** provides the introduction for this study. **Chapter 2** describes the analysis of uterine movements in infertile patients by Cine MRI images [20]. This chapter reports the identification of new uterine motion patterns and the evaluation of these patterns by visualized simulation. The relationship between the menstrual cycle and direction of movement was investigated using these new patterns. Finally, this chapter details the development of an automated CNN system for the analysis of uterine movements detected by Cine MRI. This novel system was based on feature values obtained by visualized simulation. **Chapter 3** describes the development of a diagnostic support system that predicts pregnancy outcomes by the analysis of uterine movements detected using ultrasonic images [21 and 22]. The analysis of the uterine movements was based on velocity feature values obtained from the simulations performed in **Chapter 2**. The system was composed of a CNN. **Chapter 4** presents the scientific significance and potential contribution of the novel research in this thesis.

Chapter 2

Analysis of Uterine Movement in Infertile Patients by Cine MRI Images

In this chapter, uterine movements in infertile patients were analyzed using Cine MRI images. New motion patterns were defined and evaluated by visualized simulation. The relationship between menstrual cycle and the movement direction was investigated using the new patterns. Finally, an automated system using a CNN was developed to analyze uterine movements detected in Cine MRI images. The automated system was based on feature values obtained by visualized simulation.

2.1 Introduction

Uterine peristalsis assists in the transport of sperm. The direction and frequency of peristaltic movements are known to change throughout each menstrual cycle [6, 7, 8, and 9]. Figure 2-1 shows the direction of movements at each phase of the menstrual cycle. The upward movement (corpus to fundus) occurs in the ovulation phase, the downward movement (fundus to corpus) occurs in the menstrual phase, whereas there are no movements in the luteal phase. However, random and mixed movements occur in all phases of this cycle in infertile patients. These peculiar characteristics of infertile patients were observed because of advances in MRI technology in recent years.

Table 2-1 shows uterine movements of infertile patients obtained by an MRI scanner conducted as preliminary research. The phases of the menstrual cycle and associated peristaltic directions shown in Table 2-1 were determined by physicians using patient data. The frequency shown in Table 2-1 was measured using a semi-automated technique [23] and 14 sagittal plane MRI data described in section **2.2.1 Materials**. Comparisons of uterine movement directions and frequencies between healthy subjects and infertile patients are presented in Tables 2-2 and 2-3, respectively. Table 2-2 shows the proportion of data with confirmed movement in the datasets. Data from healthy subjects were analyzed by three radiologists, as described in reference [9]. Data from

infertile patients were analyzed by the author. In the periovulatory phase, data from patients with infertility had more movements than healthy subjects. Table 2-3 shows the average frequencies of confirmed movements, which were similar in infertile patients and healthy subjects. However, the direction of uterine movement in infertile patients was different compared with those in healthy subjects, as shown in Table 2-2. These results suggest that it is difficult to assess unique characteristics of infertile patients using the same movement categories as healthy subjects, because the findings for infertile patients were markedly different compared with those from healthy subjects.

   To date, uterine movements in patients with infertility have not been investigated in detail. Therefore, it is not known which movement has negative effects on obtaining pregnancy. To clarify the characteristic uterine movements in patients with infertility, it was necessary to develop a new evaluation technique. The purpose of this study was to classify complicated uterine movements obtained by Cine MRI scans and investigate the relationship between uterine peristalsis and female infertility. While the direction and frequency of uterine peristalsis for healthy subjects were mainly evaluated in previous studies [9], this current research aimed to further examine these endpoints by new clustering patterns of uterine movements in infertile patients. Furthermore, this study aimed to develop a system that automatically analyze and classify movements detected from Cine MRI images.
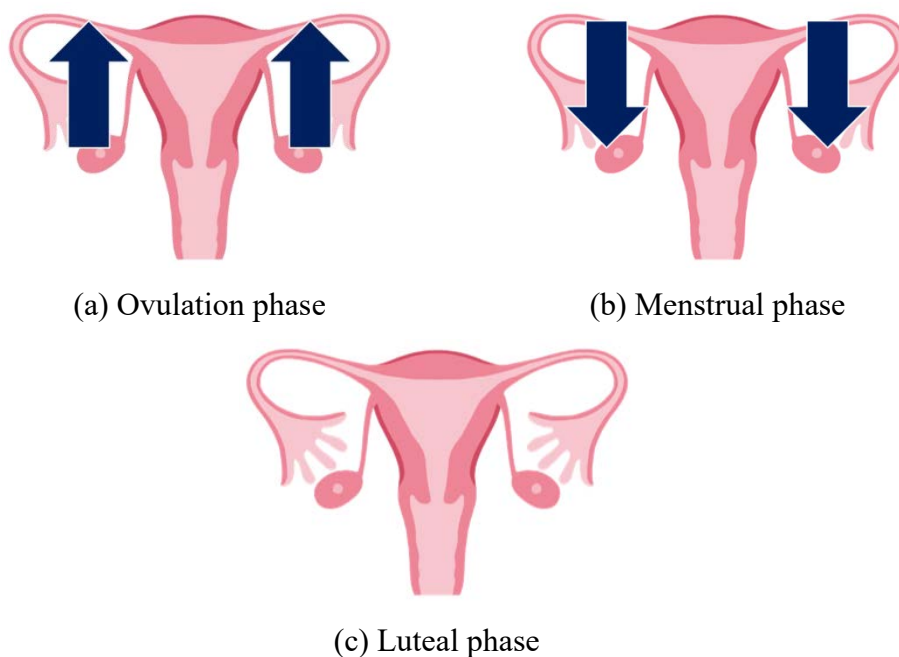
(a) Ovulation phase   (b) Menstrual phase

(c) Luteal phase

Figure 2-1 Direction of uterine movements at each phase of the menstrual cycle.

Table 2-1 Uterine movements in infertile patients [20].

No.	Menstrual cycle	Ideal movement direction	Frequency (waves/min)		
			Upward	Downward	Total
1	luteal phase	none	0.7	0.0	0.7
2	menstrual phase	downward	0.0	0.0	0.0
3	luteal phase	none	0.0	0.0	0.0
4	periovulatory phase	upward	0.0	1.0	1.0
5	follicular phase	upward	2.3	0.0	2.3
6	periovulatory phase	upward	0.0	0.0	0.0
7	periovulatory phase	upward	0.0	0.0	0.0
8	periovulatory phase	upward	0.7	0.3	1.0
9	periovulatory phase	upward	0.0	0.0	0.0
10	periovulatory phase	upward	3.7	1.0	4.7
11	periovulatory phase	upward	1.3	1.0	2.3
12	periovulatory phase	upward	0.7	0.7	1.4
13	luteal phase	none	0.0	0.0	0.0
14	periovulatory phase	upward	1.7	0.3	2.0

Table 2-2 Comparison of direction of uterine movements in menstrual cycle phases [20].

		Follicular phase	Periovulatory phase	Luteal phase	Menstrual phase
U	Healthy [9]	0.36 (5/14)	0.31 (4/13)	0.17 (2/12)	0.20 (3/15)
	Infertile	1.00 (1/1)	0.56 (5/9)	0.33 (1/3)	0.00 (0/1)
D	Healthy [9]	0.00 (0/14)	0.00 (0/13)	0.25 (3/12)	0.40 (6/15)
	Infertile	0.00 (0/1)	0.67 (6/9)	0.00 (0/3)	0.00 (0/1)

U = upward movement, D = downward movement.

Table 2-3 Comparison of average frequency (wave/min) of uterine movements in menstrual cycle phases [20].

	Follicular phase	Periovulatory phase	Luteal phase	Menstrual phase
Healthy [9]	1.2 (N = 5)	2.3 (N = 4)	1.8 (N = 4)	1.3 (N = 8)
Infertile	2.3 (N = 1)	2.1 (N = 6)	0.7 (N = 1)	- (N = 0)

2.2 Materials and Methods

2.2.1 Materials

Cine MRI images were obtained from 11 infertile female patients at different stages of the menstrual cycle. Table 2-4 shows the detail of the data of Cine MRI images. These images were taken to the SORA no MORI CLINIC. In total, 26 MRI images (14 sagittal plane and 12 transverse plane images) were obtained using a "PHILIPS Achieva 1.5T". The detection conditions used for MRI were as follows: repetition time (TR) = 2000 ms, echo time (TE) = 85 ms, Fast image = turbo spin echo (TSE), shot mode = single-shot, field of view (Fov) = 220 mm, Matrix scan = 188, exposure time = 180 s (90 serial images), cine mode display = 30 F/s and image size = 960×819 pixels. All study participants provided informed consent, and the study was approved by the ethics committee of SORA no MORI CLINIC.

2.2.2 Methods

Figure 2-2 shows the flowchart of the analysis method. In this thesis, uterine movements were analyzed following the procedures in Figure 2-2. The uterine movements detected in the 26 Cine MRI images were categorized into classes by visual analysis based on characteristic motility forms and directions of the Cine MRI images. To confirm the accuracy of clustering results, each class movement was mimicked by visualized simulation. The real MRI images were compared with the simulation images, and the mimicked movements was evaluated by four physicians. In this study, simulation had a visual aspect, and did not involve an energy calculation. The simulation parameter was set to appropriate value, and the uterine movements were evaluated using the defined classes. The presence or absence of each class of movement was visually analyzed for the 26 MRI images. Statistical characteristics of the uterine movements were examined. Finally, a system was developed that automatically extracts uterine movements of defined classes from the Cine MRI images. This system was composed of a CNN and used features obtained by the simulation and analysis.

Table 2-4 Magnetic resonance imaging (MRI) details of the data [20].

Number of MRI images for menstrual cycle stages											
Follicular phase			Periovulatory phase			Luteal phase			Menstrual phase		
S	T	To	S	T	To	S	T	To	S	T	To
1	1	2	9	7	16	3	3	6	1	1	2

S = sagittal plane, T = transverse plane, To = total.

```
┌─────────────────────────────────┐
│   Generating classes of movement │
│        for infertile patients    │
└─────────────────────────────────┘
                  │
                  ▼
┌─────────────────────────────────┐
│   Mimicking each class of movement│
│        by visualized simulation  │
└─────────────────────────────────┘
                  │
                  ▼
┌─────────────────────────────────┐
│       Analyzing correctness      │
│        of generated classes      │
└─────────────────────────────────┘
                  │
                  ▼
┌─────────────────────────────────┐
│     Evaluating uterine movements │
│           using the classes      │
└─────────────────────────────────┘
                  │
                  ▼
┌─────────────────────────────────┐
│    Developing automated movement │
│           analyzing system       │
└─────────────────────────────────┘
```
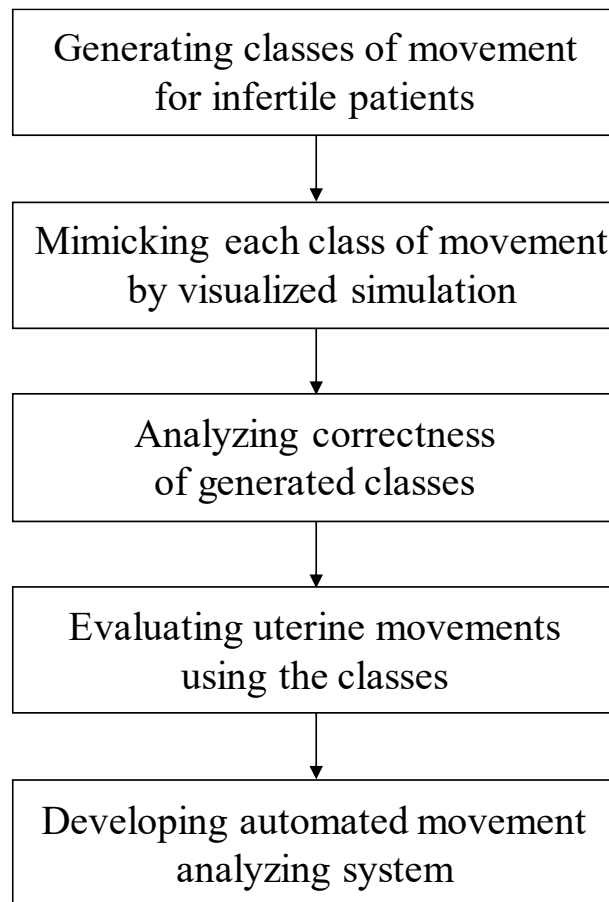
Figure 2-2 Flowchart of study.

2.3 Classification of Uterine Movements

The uterine movements were classified into classes by analysis of characteristic motility form and direction found in MRI images. The analysis found that all uterine movements in infertile patients consisted of three fundamental classes as follows: (i) a low-intensity wave that spread from the myometrium as circular wave; (ii) a low-intensity wave that moved between the endometrium and perimetrium as a band wave; (iii) a wave that wiggled along the endometrium. Each fundamental movement was classified into two types based on the directions of motion for each movement. The direction of motion from the corpus to fundus was regarded as a forward direction, and from the fundus to corpus as an opposite direction. The notations C1a, C2a and C3a denoted the forward waves of class (i), (ii) and (iii) movements, respectively. The notations C1b, C2b and C3b denoted the opposite waves of class (i), (ii) and (iii) movements, respectively. These six fundamental movements and their images are shown in Figures 2-3 and 2-4, which show sagittal and transverse planes, respectively.
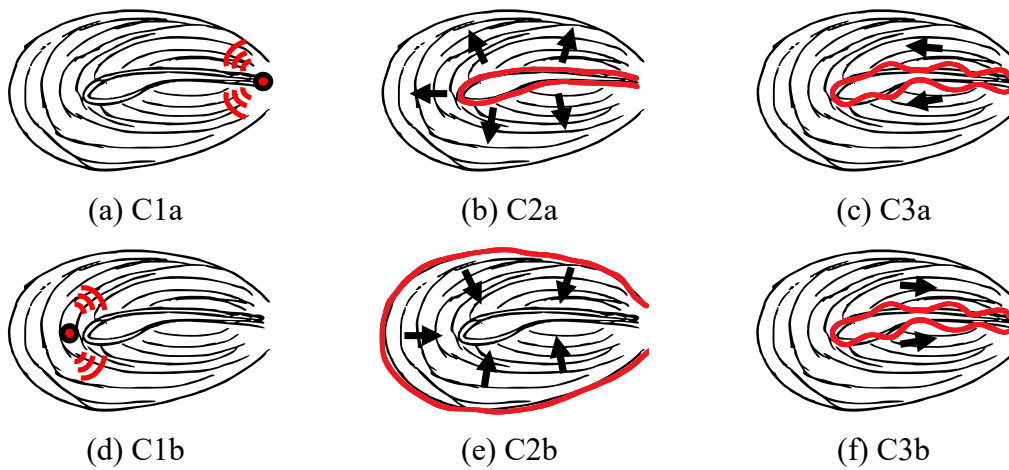
(a) C1a   (b) C2a   (c) C3a

(d) C1b   (e) C2b   (f) C3b

Figure 2-3 Images of six classes of movement (sagittal plane) [20].

(a) C1a   (b) C2a   (c) C3a

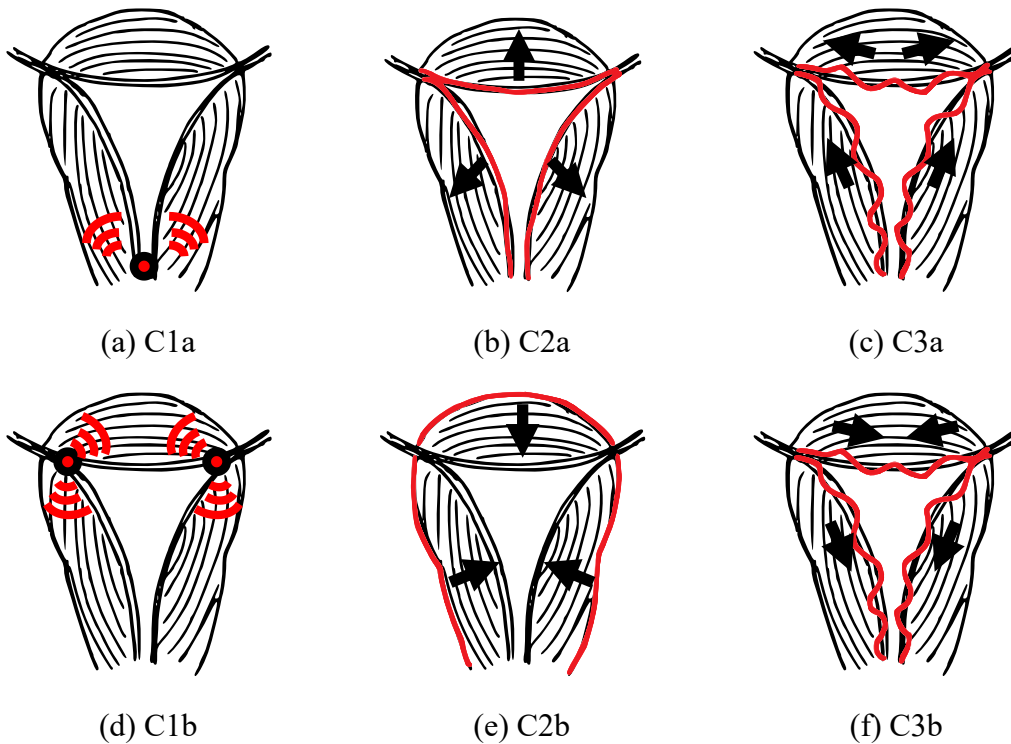(d) C1b   (e) C2b   (f) C3b

Figure 2-4 Images of six classes of movement (transverse plane) [20].

2.4 Visualized Simulation

Computer simulation was performed to mimic all uterine movements. Comparison of MRI images with computer simulation results demonstrated that the above classification successfully mimicked all the movements.

2.4.1 Simulation Model

The simulation method was based on the three-dimensional finite difference time domain (FDTD) method with a wave equation [24]. Equation (2-1) is the equation of continuity and Equation (2-2), (2-3) and (2-4) are the equations of motions.

$$\frac{\partial P(t,x,y,z)}{\partial t} = -k\frac{\partial u(t,x,y,z)}{\partial x} - k\frac{\partial v(t,x,y,z)}{\partial y} - k\frac{\partial w(t,x,y,z)}{\partial z} \qquad (2\text{-}1)$$

$$\frac{\partial u(t,x,y,z)}{\partial t} = -\frac{1}{\rho}\frac{\partial P(t,x,y,z)}{\partial x} \qquad (2\text{-}2)$$

$$\frac{\partial v(t,x,y,z)}{\partial t} = -\frac{1}{\rho}\frac{\partial P(t,x,y,z)}{\partial y} \qquad (2\text{-}3)$$

$$\frac{\partial w(t,x,y,z)}{\partial t} = -\frac{1}{\rho}\frac{\partial P(t,x,y,z)}{\partial z} \qquad (2\text{-}4)$$

P denotes stress, and u, v, and w represent velocity of the x, y and z directions, respectively. K represents bulk modulus and ρ signifies density. Figure 2-5 shows the uterine shape models in the simulation. Figure 2-5 (a) shows the x-y plane in the center of the z-coordinate. Figure 2-5 (b) shows the z-y plane in the center of the x-coordinate. The six fundamental movements were mimicked by inputting point and surface vibrations at the red area shown in Figure 2-6. The point vibration in Figure 2-6 (a) mimics the circle waves of C1a and C1b. The surface vibration in Figure 2-6 (b) mimics the band waves of C2a and C2b. The surface vibration in Figure 2-6 (c) with different phases and coordinates mimics the wiggly movements of C3a and C3b. Figure 2-7 shows the simulation results for the six fundamental movements as transverse planes of the x-y plane in the center of the z-coordinate.

2.4.2 Comparison of MRI and Simulation Results

We investigated the ability of the simulation model to mimic all uterine movements by the combination of C1a, C2a, C3a, C1b, C2b and C3b movements. The comparison was
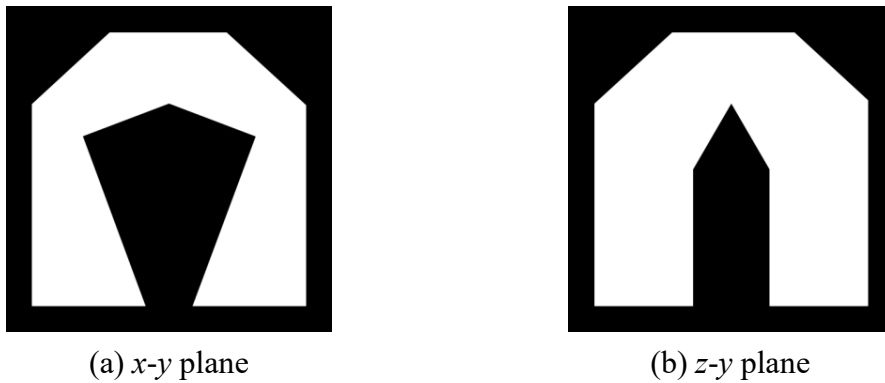

(a) *x-y* plane   (b) *z-y* plane

Figure 2-5 Simulation models of the uterus [20].

| (a) C1a and C1b | (b) C2a and C2b | (c) C3a and C3b |

Figure 2-6 Input coordinates [20].

| (a) C1a | (b) C2a | (c) C3a |

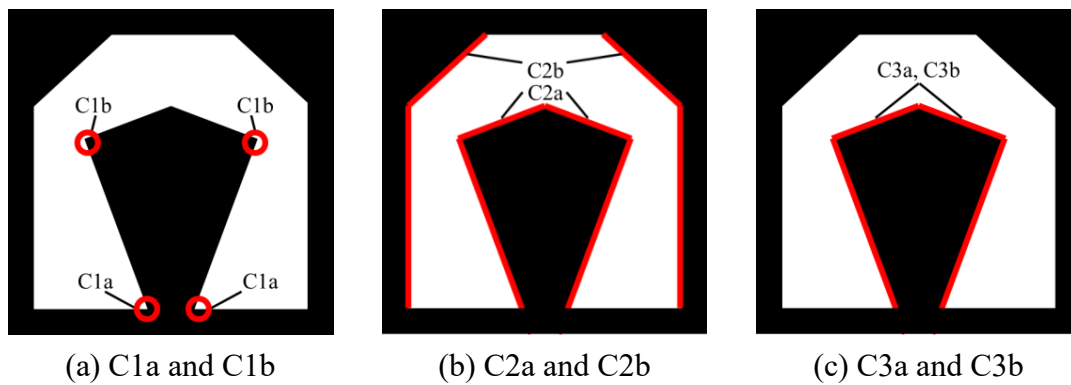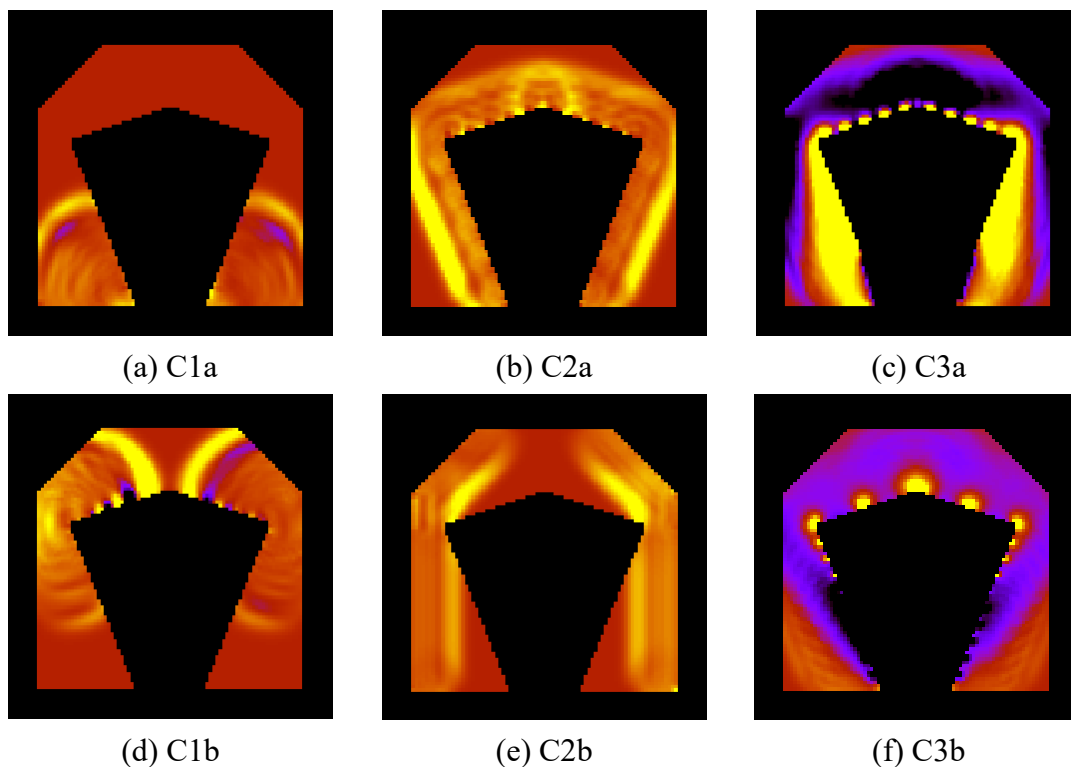| (d) C1b | (e) C2b | (f) C3b |

Figure 2-7 The six classes of movement by simulation [20].

evaluated by four physicians. If evaluators indicated that the simulation result mimicked uterine movements, the six movement patterns were considered effective to assess unique characteristics of infertile patients.

Examples of the MRI images used to compare with the simulation results are shown in Figures 2-8, 2-9, 2-10, 2-11 and 2-12. Table 2-5 shows the simulation conditions. In this study, energy was not calculated because each simulation was a visual analysis. Therefore, the simulation parameters shown in Table 2-5 show define the appropriate values without specific physical measures. In Figures 2-8, 2-9, 2-10, 2-11 and 2-12, the left MRI images correspond to the simulation images on the right. In the comparisons, we used movie files with 3 seconds generated from MRI (sampling cycle: 2 s, FPS: 30 f)

and simulation (sampling cycle: 4 us, FPS: 30 f) images. The 3D movies are not shown in this thesis. A time series of the simulation results is shown in the **Appendix** section. Four physicians compared the Cine MRI and simulated images by direct observation, and found that the simulated images successfully mimicked all 26 Cine MRI images. This analysis demonstrated that the six movement patterns were effective at assessing the unique uterine characteristics of infertile patients.
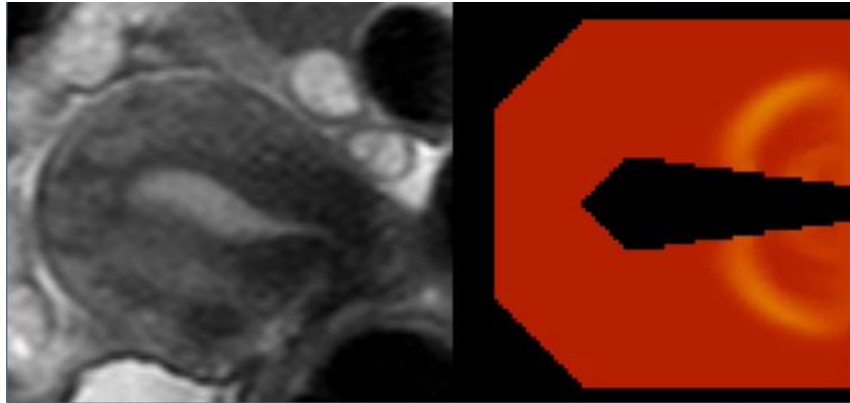

Figure 2-8 Comparison on pattern 1 (C1a) [20].
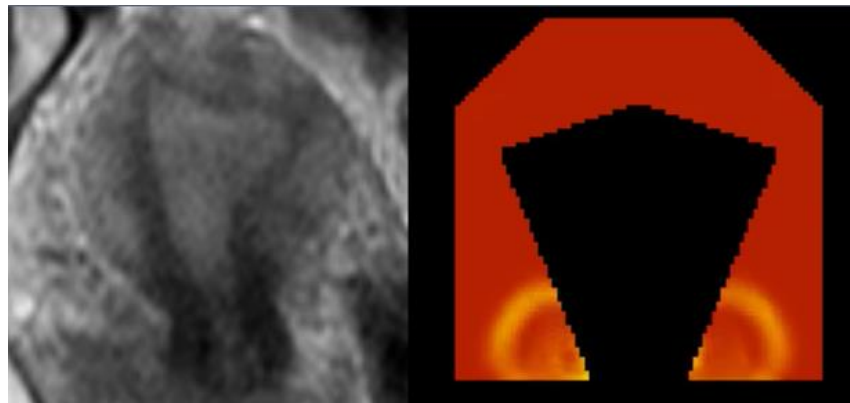
Figure 2-9 Comparison on pattern 2 (C1a) [20].
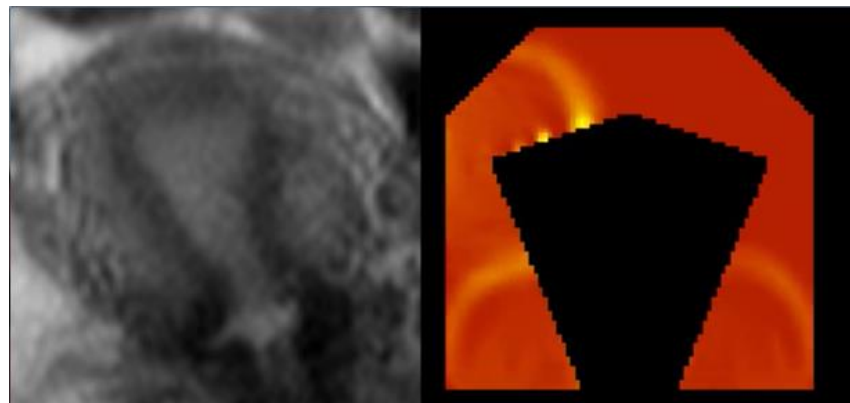
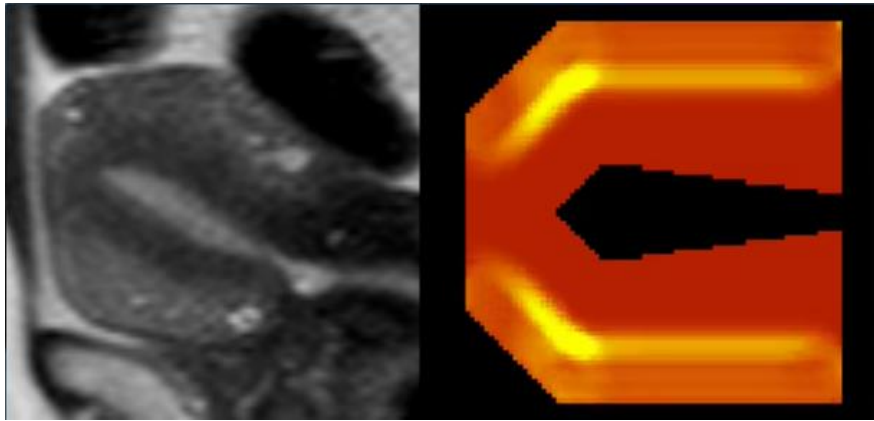Figure 2-10 Comparison on pattern 3 (C1a and C1b) [20].

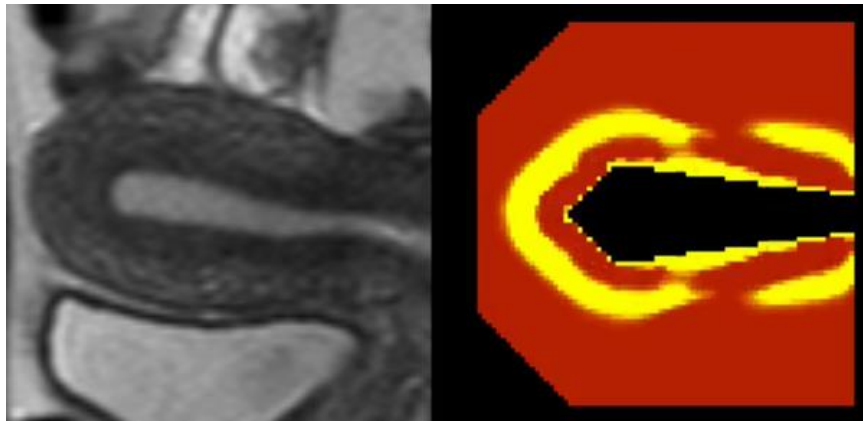Figure 2-11 Comparison on pattern 4 (C2b) [20].

Figure 2-12 Comparison on pattern 5 (C2a and C3b) [20].

Table 2-5 Simulation conditions [20].

Density ρ	1.2 [kg/m^3]
Bulk modulus K	1.4×10^5 [N/m^2]
Propagation velocity $(K/\rho)^{1/2}$	341.6 [m/s]
Time step size	1.0×10^{-6} [s]
Number of calculation steps	360 [step]
Unit lattice size	1.0 [mm]
Boundary condition	PML
Lattice geometry	Staggered grid
Number of grid points	$100 \times 100 \times 100$

The simulation mimicked all uterine movements without changing the propagation velocity. The recording time was 0.36 ms and the propagation velocity was 341.6 m/s in the simulation. This study found that the propagation velocity in the MRI images was 0.68 mm/s, as determined by Equation (2-5).

$$V = 341.6 \times (0.36 \times 10^{-3}/180.0) = 0.68 \times 10^{-3} \qquad (2\text{-}5)$$

14

The propagation velocity of uterine peristalsis had been not reported. The current simulation analysis revealed that the propagation velocity of uterine peristalsis exhibited a constant velocity of 0.68 mm/s.

2.5 Evaluation of Experimental Results

The direction of uterine motion in MRI images was compared with the ideal direction (described below) of uterine motion. The direction information was obtained by directly inspecting each image for the presence or absence of each class of movement. The author analyzed 26 MRI images by direct observation. The ideal direction was based on the stage of the menstrual cycle of the patient defined by physicians. The observed motion directions were determined to coincide with the ideal direction when the any of the following conditions was satisfied: (1) Generated movements were only C1a, C2a, or C3a when the ideal direction was a forward movement. (2) Generated movements were only C1b, C2b, or C3b when the ideal direction was an opposite movement. (3) Generated movements were none when the ideal direction was none.

In Table 2-6, notation "1" represents the presence of movement and "-" indicates the absence of movement. The comparison found that the direction of uterine motion for 13/26 MRI images coincided with the defined stages of the menstrual cycle. Table 2-7 also summarizes the cases where the motion direction never coincided with the defined stage of the menstrual cycle, and shows that these motion classes were only C1a, C1b and C3b. It was speculated that motions C1a and C1b affect the ideal direction. Analysis of these findings using a 2×2 contingency table (Table 2-8) and the chi-square test found a test statistic $T = 3.94$. The value of the chi-square distribution was 3.84 when the degrees of freedom $n' = 1$ and the significance level was 0.05. It was concluded that C1a and C1b were wrong motions with $T > 3.84$.

2.6 Automated Analyzing System for Uterine Movement

This study developed an automated analyzing system for uterine movements. The system predicts the class of uterine movement from Cine MRI images by the velocity information for the uterine movement. The analysis of the system was based on the key feature obtained by visualized simulation, showing that all uterine peristalsis exhibited a constant propagation velocity. Two CNN models were developed to evaluate the automatic system. One was composed of the original Cine MRI images (shape-based system) and the other was composed of images with velocity information (velocity-based system). Experimental comparison evaluated the prediction accuracy of movement types.

Table 2-6 Observed uterine movements [20].

	P	I	C1a	C1b	C2a	C2b	C3a	C3b	Co
1	Sa	a	-	-	1	-	-	1	F
2	Sa	a	-	-	-	-	1	-	T
3	Tr	a	-	-	-	-	1	-	T
4	Sa	a	-	-	1	-	1	-	T
5	Tr	a	-	-	1	-	1	-	T
6	Sa	a	-	-	1	-	1	-	T
7	Tr	a	-	-	-	-	1	1	F
8	Sa	a	1	-	1	-	-	-	T
9	Tr	a	-	-	1	-	1	-	T
10	Sa	a	-	-	1	-	1	-	T
11	Sa	a	1	-	-	-	-	-	T
12	Sa	a	1	1	-	-	-	-	F
13	Tr	a	1	1	-	-	1	-	F
14	Tr	a	1	-	-	-	-	-	T
15	Sa	a	1	1	-	-	-	-	F
16	Tr	a	-	-	-	-	1	1	F
17	Tr	a	-	-	-	-	1	1	F
18	Sa	a	1	-	-	-	1	1	F
19	Tr	b	1	1	-	-	-	-	F
20	Sa	b	-	-	-	1	-	-	T
21	Sa	N	1	-	-	-	-	-	F
22	Tr	N	1	-	-	-	-	-	F
23	Tr	N	1	-	-	-	-	-	F
24	Sa	N	1	-	-	-	-	-	F
25	Sa	N	-	-	-	-	-	-	T
26	Tr	N	-	-	-	-	-	-	T

P: plane type, Sa = sagittal plane, Tr = transverse plane. I: ideal direction, a = forward movement, b = opposite movement, N = none. Co: coincided, T = true, F = false.

2.6.1 Methods

Two types of CNN models were developed; a shape-based and velocity-based model. Figure 2-13 shows that the structure of the CNN models included a combination of VGG16 [14] and fully connected layers. This study used VGG16 that had been previously established by ImageNet [25].

Table 2-7 Patients with classes of uterine motions that did not coincide with expected movements [20].

Patient No.	Generated waves	Direction of correct motion in menstrual cycle	Class with no coincidence
1	C2a and C3b	forward	C3b
7	C3a and C3b	forward	C3b
12	C1a and C1b	forward	C1b
13	C1a, C1b and C3a	forward	C1b
15	C1a and C1b	forward	C1b
16	C3a and C3b	forward	C3b
17	C3a and C3b	forward	C3b
18	C1a, C3a and C3b	forward	C3b
19	C1a and C1b	opposite	C1a
21	C1a	none	C1a
22	C1a	none	C1a
23	C1a	none	C1a
24	C1a	none	C1a

Table 2-8 Contingency table [20].

	Coincided	No coincidence	Total
(C1a OR C1b)	3	8	11
NOT (C1a AND C1b)	10	5	15
Total	13	13	26
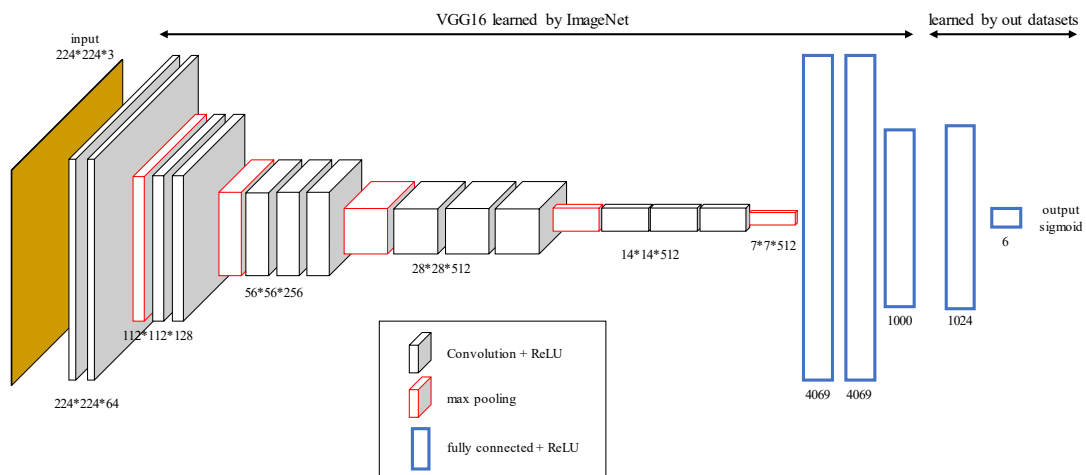
Figure 2-13 Convolution Neural Network (CNN) architecture [20].

2.6.1.1 Shape-based Model

This section describes a shape-based system using a CNN. The system extracted information of endometrium shape by convolution layers and predicted movement types.

Images were prepared as input for the CNN model. The uterine region was extracted from Cine MRI images by a mask image manually generated in advance. Figure 2-14 shows an original image, a mask image, an image extracted by the mask, and a resized image. Because uterine shape and direction have individual variation between patients, extracted region sizes were different from each other. Rotation processes every 30 degrees from −90 to +90, and every 10 degrees from −30 to +30, were applied to extracted images in the sagittal and transverse planes, respectively. Obtained images were saved at 224×224 pixels. Figure 2-14 (d) shows a saved image at 224×224 pixels. Figure2-15 shows examples of saved images. Figure 2-15 (a) and (b) panels show examples of saved Cine MRI images, with original images collected one time step apart shown in the center vertical columns, and the left and right side images showing rotated images for the original center images.

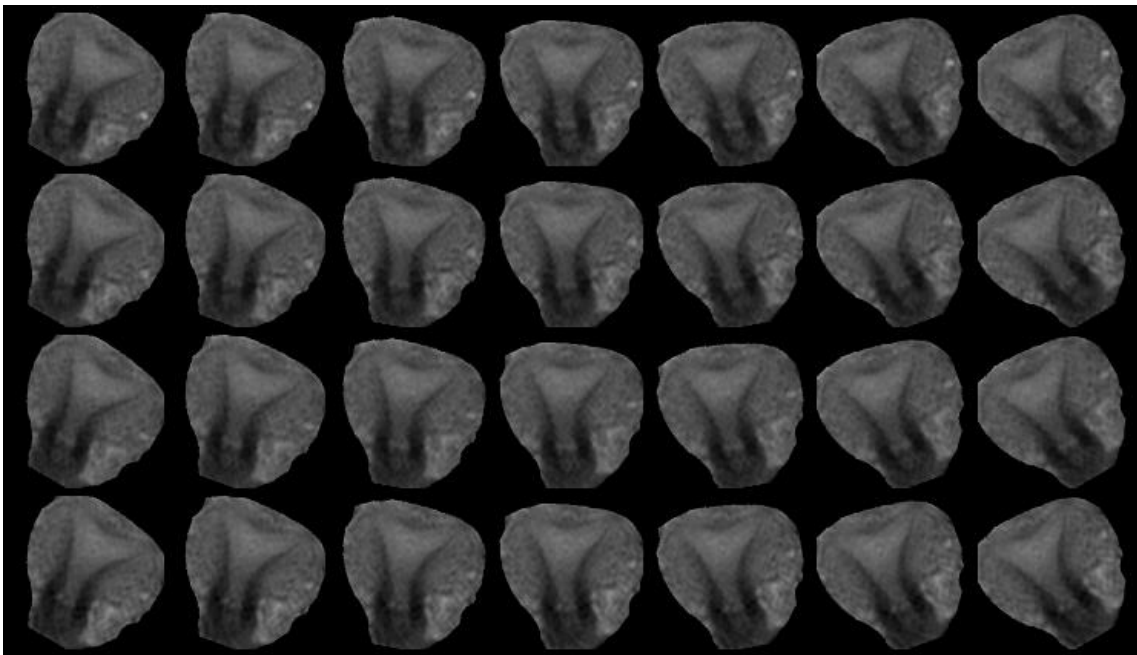|	
(a) Original image	(b) Mask image
(c) Extracted image	(d) Resized image
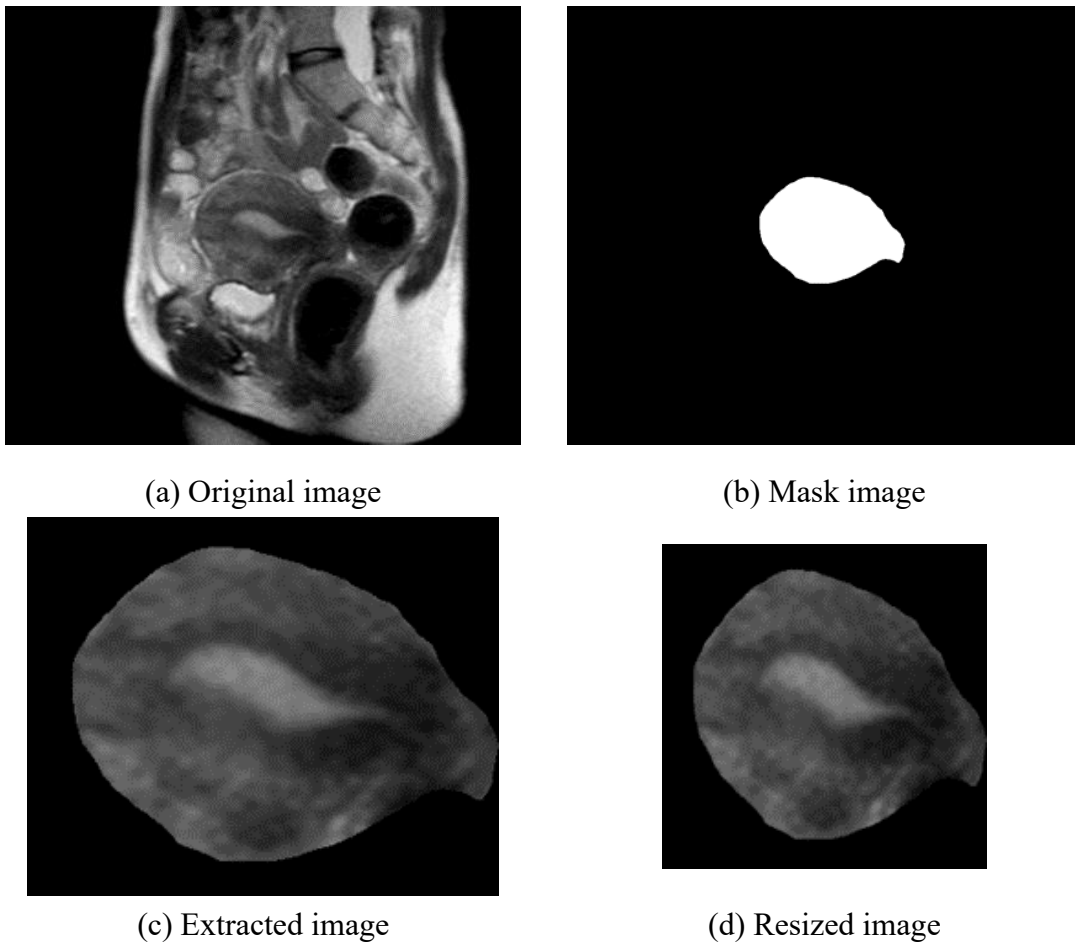
Figure 2-14 Examples of the saved images.
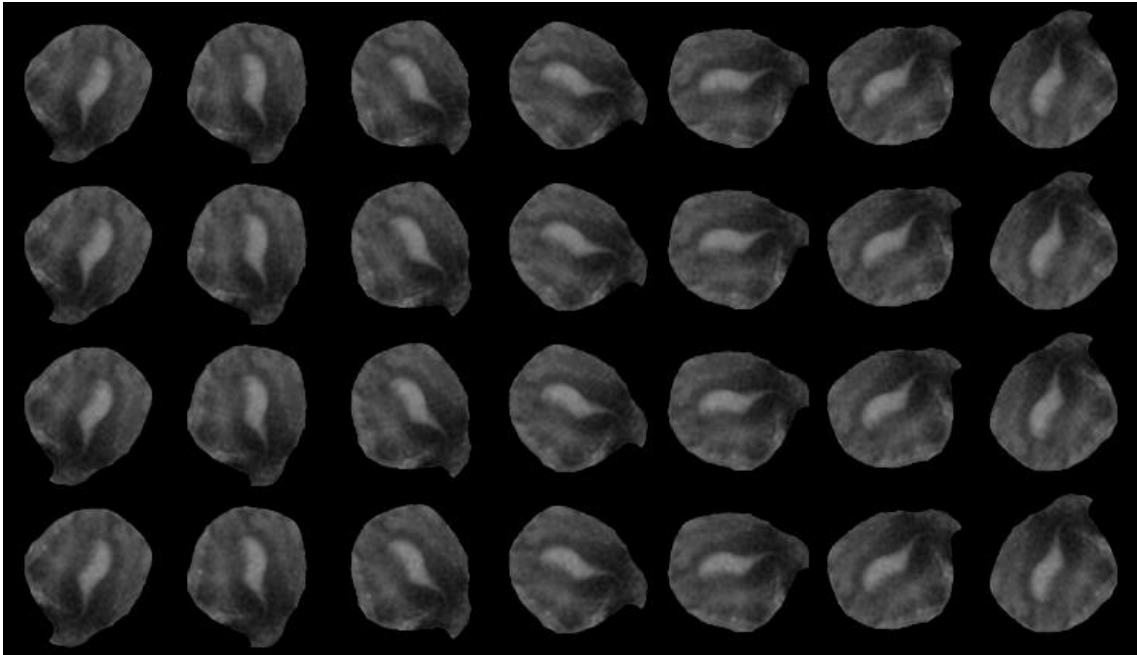
(a) Sagittal plane

(b) Transverse plane

Figure 2-15 Examples of the saved Cine MRI images.

2.6.1.2 Velocity-based Model

This section describes the velocity-based prediction model using a CNN. The system predicts the classes of uterine movement by analyzing images with velocity information.

Images were prepared as input for the CNN model. An averaging filter of 30×30

pixels was applied to the images generated in **Section 2.6.1.1**. Interframe differences *Diff*(*t*, *x*, *y*) were calculated for the images, and the values of *Diff*(*t*, *x*, *y*) were converted to *Diff'*(*t*, *x*, *y*) according to Equation (2-6).

If $Diff(t, x, y) \leq 0$:

$$Diff'(t, x, y) = 0$$

Else $Diff(t, x, y) \leq 20$:

$$Diff'(t, x, y) = \frac{Diff(t, x, y)}{20} \times 255 \qquad (2\text{-}6)$$

Else:

$$Diff'(t, x, y) = 255$$

t denotes a frame number, and *x* and *y* represent a *x*- and *y*-coordinate points in the image. Since 99.7 percent values of *Diff*(*t*, *x*, *y*) in the dataset was 20 or less, the number 20 was used in Equation (2-6). *Diff'*(*t*, *x*, *y*) was applied to a moving average filter of five points for the *t*-axis direction. Optical flow was calculated for adjacent frames of *Diff'*(*t*, *x*, *y*). The optical flow was calculated by the Farneback method [26]. The displacement of each pixel *D*(*t*, *x*, *y*) was calculated from the results of the optical flow. A velocity image *V* was generated by the Equation (2-7).

If $1 - |3.5 - D(t, x, y)|/2 \leq 0$:

$$V(t, x, y) = 0$$

Else: $\qquad (2\text{-}7)$

$$V(t, x, y) = \left(1 - \frac{|3.5 - D(t, x, y)|}{2}\right) \times 255$$

Here, the numbers 3.5 and 2 were values obtained from an average value and a standard deviation of *V*(*t*, *x*, *y*) in the dataset. Images were saved as images with velocity information by converting the brightness values to *V*. Figure 2-16 shows examples of the saved images.

2.6.2 Comparative Experiments

Labels for the images had six types of movements labeled as C1a, C1b, C2a, C2b, C3a, and C3b. These movements may occur simultaneously or not at all. Therefore, the model utilized multi-label classifications. Label information were set according to Table 2-6. The output was sigmoidal and the system was evaluated by *k*-fold cross validation with *k* = 3. The sagittal plane images from 14 patients were divided into three groups, and transverse plane images from 12 patients were also divided into three groups. Tables 2-9 and 2-10 show the results of divided sagittal and transverse plane images, respectively. The images from one group were extracted from the dataset as validation data, and the model used the images from the remaining two groups as training data. Images that were
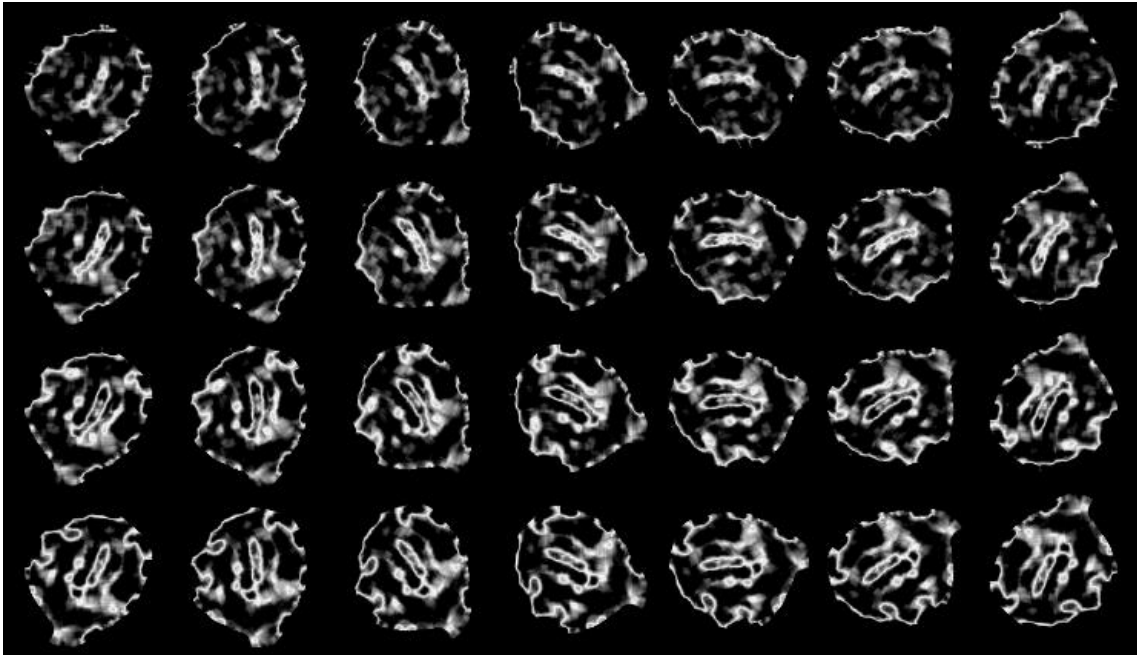
(a) Sagittal plane
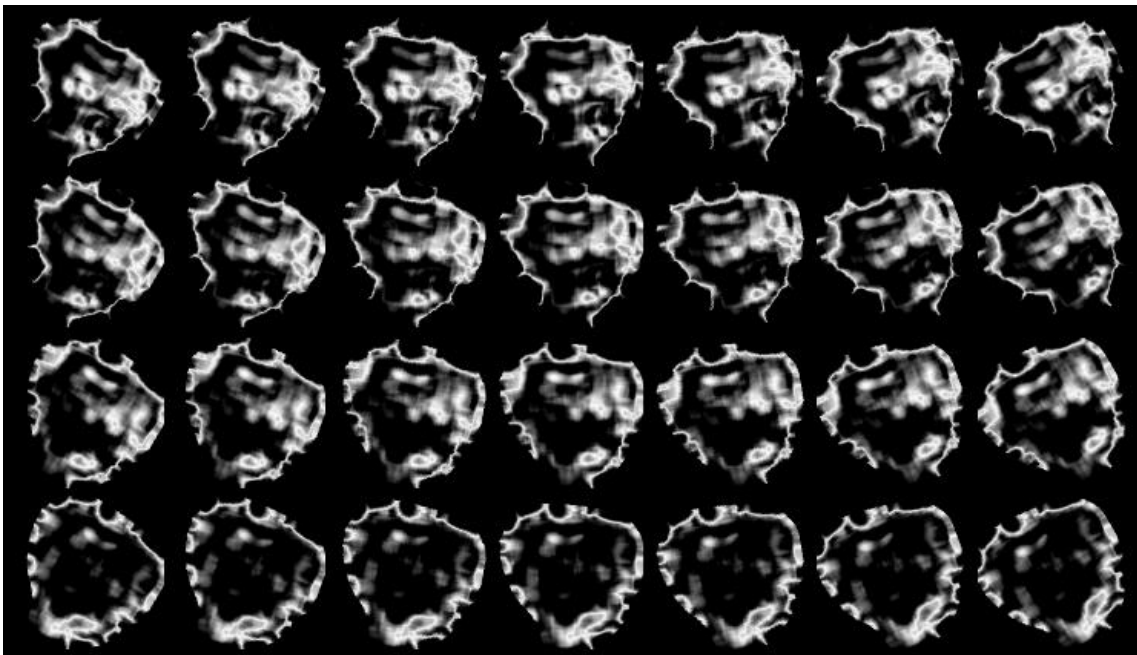
(b) Transverse plane

Figure 2-16 Examples of images saved with velocity information.

not rotated in the validation data were used as test data. The model learns during 20 epochs. The k-fold cross validation repeated the learning while groups were changed for validation data, until all groups were used for validation data. Therefore, we obtained three learning curves and prediction results for all patients' data.

Table 2-9 The subjects for groups in the sagittal plane dataset.

	Group 1	Group 2	Group 3
Subject numbers	1, 2, 20, 21, 24	6, 8, 10, 11, 12	4, 15, 18, 25
Number of images	2,870	3,080	2,464
Total	8,414		

Table 2-10 The subjects for groups in the transverse plane dataset.

	Group 1	Group 2	Group 3
Subject numbers	3, 19, 22, 23	7, 9, 13, 14	5, 16, 17, 26
Number of images	2,464	2,254	2,464
Total	7,182		

Figures 2-17 and 2-18 show the learning curves for accuracy and loss of validation data for the sagittal plane images. In Figures 2-17 and 2-18, the horizontal axis shows the number of epochs, and the vertical axes show the accuracy and loss. The accuracy was binary and the loss was categorical cross entropy. The velocity-based model had a higher accuracy than the shape-based model (Figure 2-17), and a lower loss compared with the shape-based model (Figure 2-18). Based on these results, the velocity-based model provides an effective approach to predict movement types. Table 2-11 shows the accuracy and loss of the models in the final step.

Figures 2-19 and 2-20 show the learning curves for accuracy and loss of validation data for the transverse plane images. In Figures 2-19 and 2-20, there was almost no difference between the velocity-based and shape-based models. Table 2-12 shows the accuracy and loss of the models in the final step. The velocity-based model had a lower accuracy and lower loss than the shape-based model.

In the analysis of sagittal plane images, the velocity-based model obtained a higher score than the shape-based model. However, in the analysis of transverse plane images, the score of the velocity-based model was not higher than that of the shape-based model. It is possible that the cause of these results was the lack of correct information regarding the relationship between pixel and distance. Additionally, the model may have required more learning input because of larger individual differences in endometrial shape and size between transverse plane images compared with sagittal plane images.
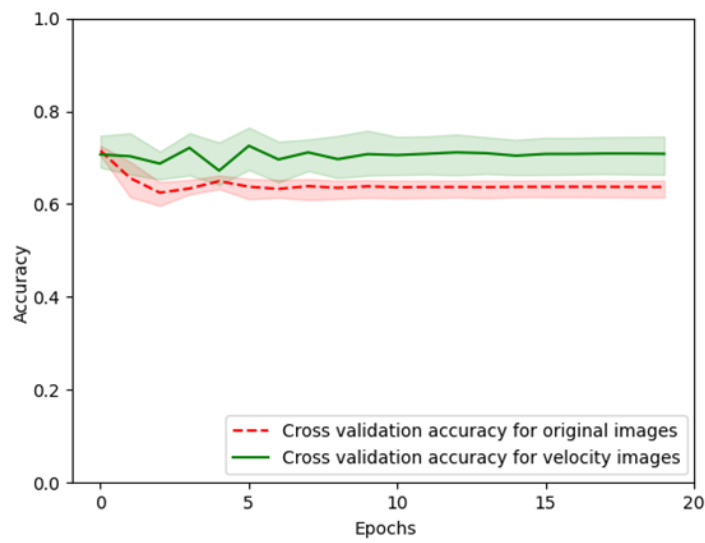
Figure 2-17 Learning curve showing cross-validation accuracy in the sagittal plane.
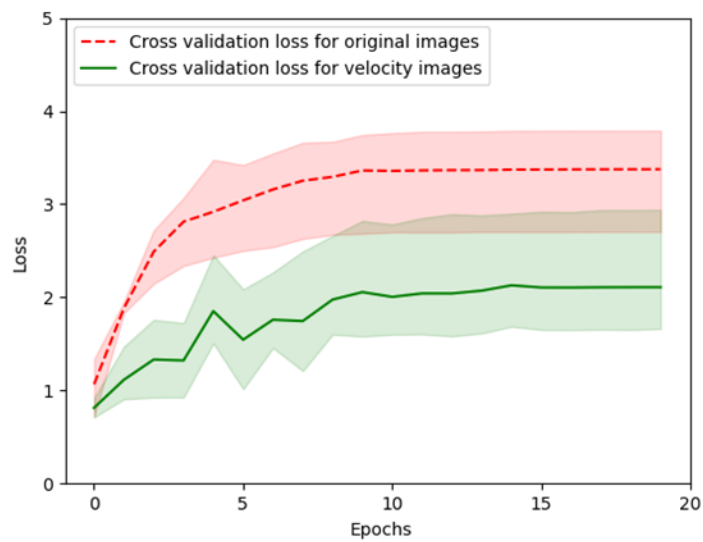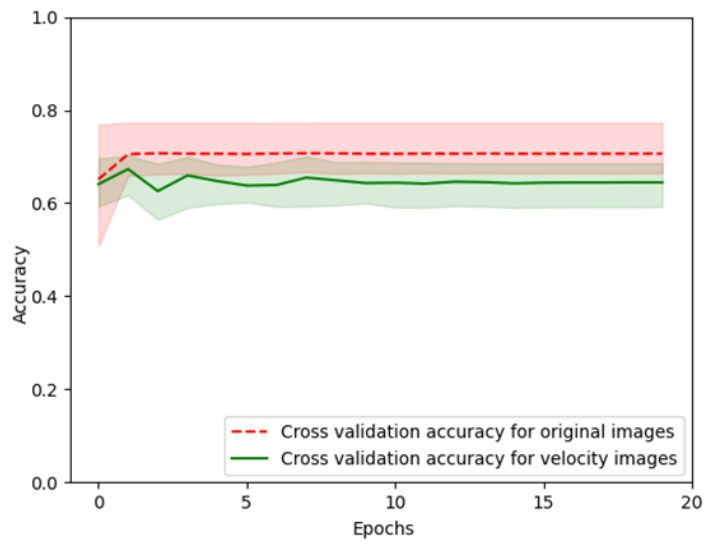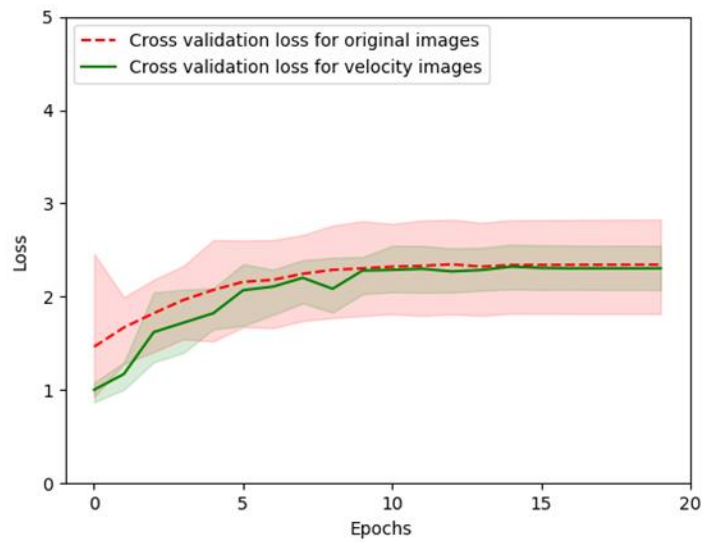

Figure 2-18 Learning curve showing cross-validation loss in the sagittal plane.

Table 2-11 Accuracy and loss of the models for the sagittal plane at the final step.

	Shape-based model	Velocity-based model
Accuracy	0.64	0.71
Loss	3.38	2.11

Figure 2-19 Learning curve showing cross-validation accuracy in the transverse plane.

Figure 2-20 Learning curve showing cross-validation loss in the transverse plane.

Table 2-12 Accuracy and Loss of the Models for the Transverse Plane at the Final Step

	Shape-based model	Velocity-based model
Accuracy	0.71	0.64
Loss	2.34	2.30

2.7 Conclusions

Uterine peristalsis is related to fertility. The direction and frequency of peristalsis corresponds to each stage of the menstrual cycle for healthy women. However, random and mixed uterine movements occur in some phases of the cycle for patients with infertility. Therefore, characteristics of the direction and frequency of uterine movements in infertile patients differ from healthy subjects. To further understand uterine peristalsis in infertile patients, we classified six fundamental uterine movements as basis for a new evaluation model. The movements were classified based on motility form and direction. Evaluation of the direction of motion identified two fundamental movements (C1a and C1b) that provide candidate factors for female infertility. These results formed the basis of an evaluation method of uterine movements for infertile patients. Visualized simulation analysis of the validity of clustering results found that all uterine peristalsis exhibited a constant propagation velocity of 0.68 mm/s. The feature will likely be applied to many studies in the field of infertility, because the current study demonstrated that a CNN system based on this velocity feature had a higher performance than a CNN system based on shape features. In sagittal plane images, the velocity-based system had a higher prediction accuracy than the shape-based system. However, the prediction accuracy of the velocity-based system was not higher than the shape-based system for transverse plane images. The differences between sagittal and transverse plane images may reflect a dataset lacking diversity because of the limited number of training data. The prediction accuracy will be improved by solving the problem of the dataset. In the future, new data augmentation methods will be investigated to improve the performance of the velocity-image based system.

Chapter 3

Pregnancy Prediction Systems by Ultrasonic Images

3.1 Introduction

Ultrasonic B-mode images are often used during infertility treatment. Endometrial shape, detected via ultrasonic images, changes during phases of the menstrual cycle [10, 11, and 12]. Before ovulation, the endometrium has a leaf-like pattern, as shown in Figure 3-1. After ovulation, the endometrium has a uniform shape, known as the homogenous pattern, as shown in Figure 3-2. Physicians evaluate the optimal phase for pregnancy outcome based on endometrial shapes. Based on the relationship between endometrial shapes and phases of the menstrual cycle, it is generally considered that a leaf pattern represents the optimal time for achieving pregnancy, and the homogenous pattern represents the time of a low pregnancy rate. Endometrial shapes in ultrasonic images are evaluated by direct observation. However, it is difficult to correctly evaluate endometrial shapes from ultrasonic images. The fertility treatment may fail even if the physician identifies a leaf pattern, and treatment may succeed even if the physician identifies a homogenous pattern.

To correctly evaluate endometrial shapes, this study developed an evaluation system for optimal uterine features based on a Local Binary Pattern (LBP) feature (described in **Section 3.3 Analyzing System by LBP**). The LBP feature utilizes values showing local shape information for an image [27 and 28], and has been mainly used for face recognition [29, 30, 31, and 32], as well as analysis of medical images [33, 34, 35, 36, and 37]. The goal of the current LBP system was to use endometrium shape information from ultrasonic images to predict the success rate of a subsequent pregnancy. However, endometrial shapes displayed on ultrasonic images are not stable because of the angle of incidence of ultrasonic waves. Furthermore, the LBP method may be affected by variations in uterine position. It is difficult to develop an automated method aligning uterine direction because of the large individual variation in endometrial shapes and sizes.
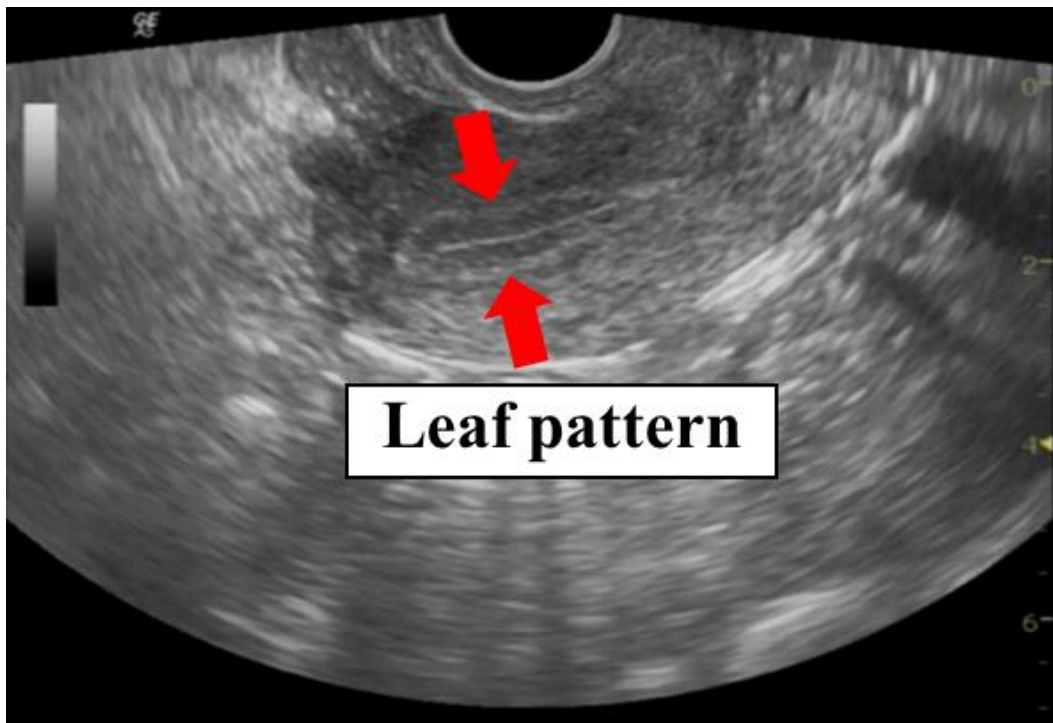
26

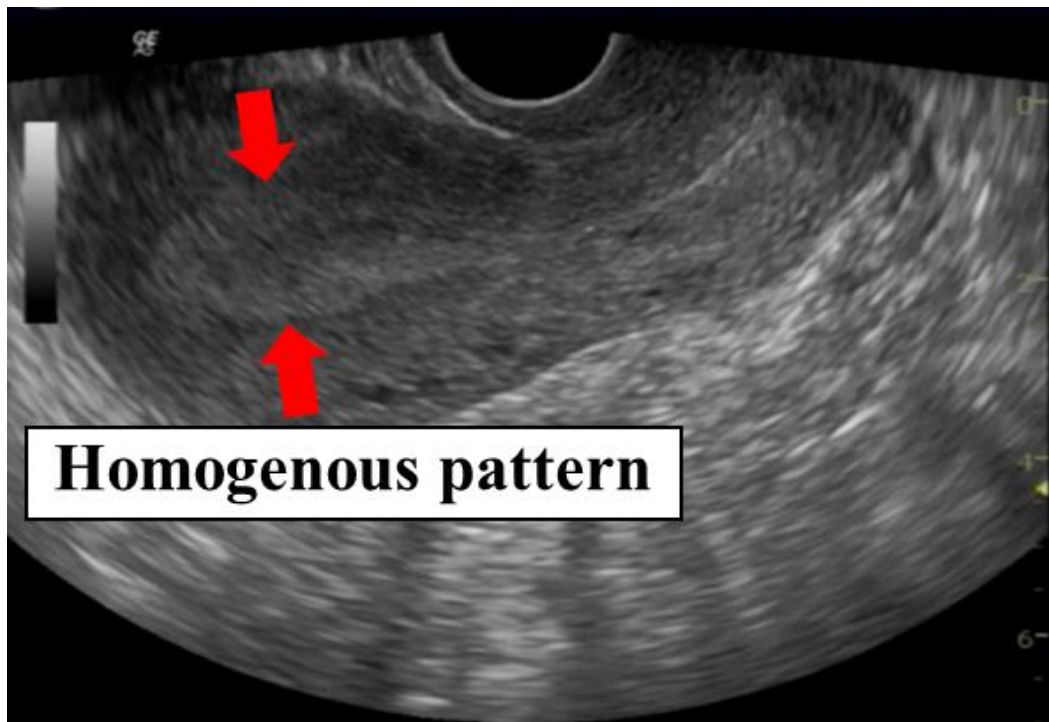Figure 3-1 Example of a leaf pattern in an ultrasound image.

Figure 3-2 Example of a homogenous pattern in an ultrasound image.

For the current analysis, uterine direction was aligned by manually rotating the images, which may be subjective. To overcome these problems with the LBP system, a new system was developed to improve the accuracy of detection of uterine features.

Uterine peristalsis assists in the transport of sperm. The direction and frequency of peristalsis changes during the phases of each menstrual cycle [6, 7, 8, and 9]. Uterine peristalsis is mainly observed using Cine MRI images, but can also be observed by ultrasonic images. Therefore, menstrual cycle information can be predicted by analyzing uterine peristalsis from ultrasonic images. As mentioned above, the endometrium exhibits different patterns via ultrasound imaging before and after ovulation. The frequency of uterine peristalsis decreases from the ovulation to luteal phase. Therefore, the frequencies of movement of the leaf and homogenous patterns must also be different. Pregnancy can be predicted by analyzing the movement, without detailed analysis of endometrial shapes.

The images shown in Figures 3-1 and 3-2 were obtained by inserting an ultrasonic probe into a vagina. The image was affected by camera shake because the probe was controlled by the physician's hand. Therefore, it was difficult to extract uterine peristalsis from the ultrasonic images. In **Chapter 2**, the findings showed that the movement velocity of uterine peristalsis was 0.68 mm/s. Therefore, it was predicted that the analysis of velocity information in ultrasonic images would allow extraction of uterine peristalsis features.

This chapter describes a pregnancy outcome prediction system based on CNN analysis of uterine movement. Accuracies of the system were compared using two information of shape and velocity. The shape-based system, based on conventional theory, predicted pregnancy using original ultrasonic images. The velocity-based system, developed in this thesis, predicted pregnancy using images generated from velocity information.

3.2 Ultrasonic Images

This chapter describes the analysis of ultrasonic B-mode images, taken at the Reproduction Clinic Osaka, of infertile female patients. The dataset included images from 38 patients. These images had leaf or homogenous patterns classified by a physician, and included patient information regarding the success or failure of a pregnancy. Table 3-1 shows the number of subjects. Because the ultrasonic images were taken in a time series for each patient, the dataset consisted of movie files. Table 3-2 shows details of the movie files. All study participants provided informed consent, and the study was approved by the ethics committee of University of Hyogo (approved number: 201901 and 202004).

Table 3-1 Number of subjects.

	Success	*Failure*	Total
Leaf	9	11	20
Homogenous	10	8	18
Total	19	19	38

Table 3-2 Detail of movie files.

Extension	mpg
Width	720 pixels
Height	480 pixels
Color mode	Gray scale
Gradation	256
Frame rate	30 fps
Record time	29-34 sec (Average: 30.8 sec)

3.3 Prediction by LBP

This section describes the development and evaluation of prediction system for pregnancy based on LBP analysis.

3.3.1 Methods

Local shape features of endometrium images were analyzed by an LBP. The LBP classified the relationship between the target pixel and peripheral pixels into 256 mask patterns. This feature was effective for images with a change in brightness values. Furthermore, the calculation cost of an LBP was very low. Figure 3-3 shows a flowchart of the analysis method. The average brightness values for the time axis direction were calculated for each pixel from the movie file, and the average image of the ultrasonic images was made for each patient. The endometrium region was extracted using the partial shape constraint contour model [38]. LBP values were calculated in the extracted endometrial region, and a histogram of the LBP values was recorded for each image. This study analyzed LBP features in the recorded histograms to develop a prediction system of pregnancy outcome.

3.3.2 Analyzing LBP Values

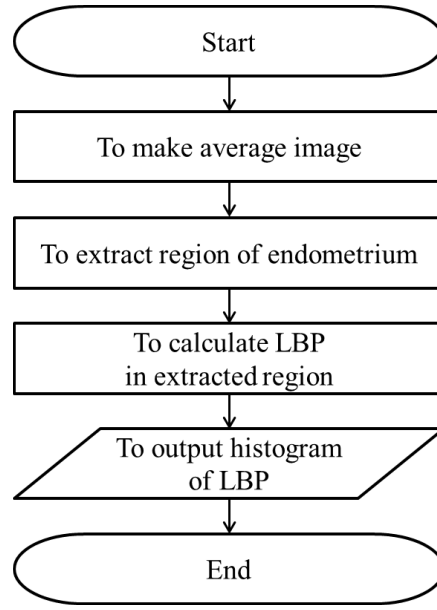The LBP value was calculated by thresholding the neighborhood of each pixel. The

```
        ┌─────────────────┐
        │      Start      │
        └────────┬────────┘
                 │
        ┌────────▼────────┐
        │ To make average image │
        └────────┬────────┘
                 │
        ┌────────▼────────┐
        │ To extract region of endometrium │
        └────────┬────────┘
                 │
        ┌────────▼────────┐
        │   To calculate LBP   │
        │  in extracted region │
        └────────┬────────┘
                 │
        ┌────────▼────────┐
        │ To output histogram │
        │      of LBP       │
        └────────┬────────┘
                 │
        ┌────────▼────────┐
        │       End       │
        └─────────────────┘
```

Figure 3-3 Flowchart of the analysis method. LBP, local binary pattern.

calculation method used Equation (3-1).

$$LBP = \sum_{p=0}^{7} s(g_p - g_c)2^p$$

$$s(g_p - g_c) = \begin{cases} 1 & g_p \geq g_c \\ 0 & g_p < g_c \end{cases}$$

$\qquad\qquad\qquad\qquad\qquad\qquad\qquad\qquad\qquad\qquad$ (3-1)

The notations g_c and g_p denote brightness values of the central pixel and its neighbor, respectively. Uterus directions in ultrasonic images were variable for each patient. Because the LBP requires angle information as a feature value, it was difficult to analyze features in the original ultrasonic images. Therefore, an LBP rotation invariant (LBP_{ri}) was used as a first step to analyze the features. In the calculation of an LBP, an eight-bit binary pattern was obtained. LBP_{ri} is the minimum value obtained by binary shifts for the eight-bit binary pattern. Figure 3-4 shows an example of an LBP_{ri}.

An LBP_{ri} was calculated for each endometrial region extracted from the average image by a mask image. The mask images were generated based on analyzing results of the partial shape constraint contour model. Figure 3-5 shows examples of the original image, mask image, and an image extracted by the mask. Figure 3-6 shows the LBP_{ri} values calculated for the datasets as a histogram. In Figure 3-6, the horizontal axis shows mask pattern number and the vertical axis indicates the frequency for each mask pattern. Notation LP denotes datasets for a leaf pattern and pregnancy, LN indicates a leaf pattern and non-pregnancy, HP shows a homogenous pattern and pregnancy, and HN denotes a homogenous pattern and non-pregnancy. In Figure 3-6, mask pattern numbers 15 and 31

have high frequencies. The shapes of mask pattern numbers 15 and 31 are shown in Figures 3-7 and 3-8, respectively. These mask patterns show edge patterns. Therefore, this analysis found that the endometrium region was mainly composed of edge mask patterns.
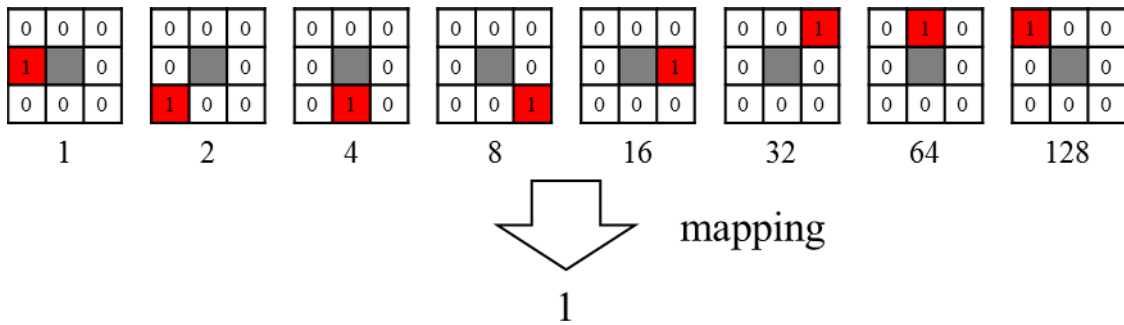

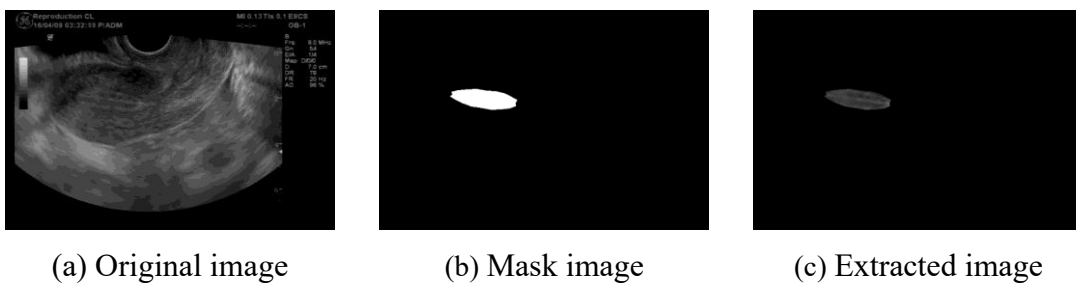Figure 3-4 Example of local binary pattern rotation invariant (LBP$_{ri}$).

(a) Original image   (b) Mask image   (c) Extracted image

Figure 3-5 Examples of uterine region extraction.
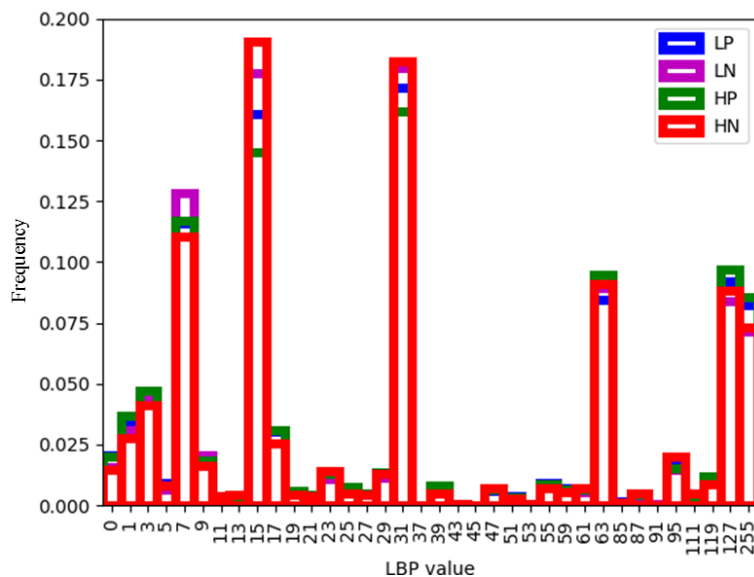
Figure 3-6 Histogram of local binary pattern (LBP) values with the rotation invariance.

L, leaf pattern. H, homogenous pattern. P, pregnancy. N, no pregnancy.
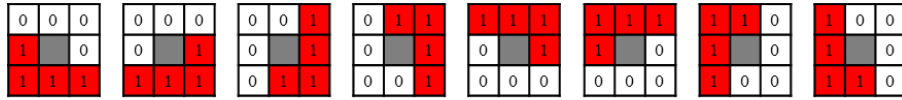
15

Figure 3-7 Shape of mask pattern number 15 in the local binary pattern rotation invariant (LBP$_{ri}$).
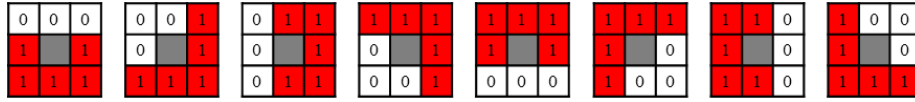
31

Figure 3-8 Shape of mask pattern number 31 in the local binary pattern rotation invariant (LBP$_{ri}$).

3.3.3 Analyzing Edge Angles

In **Section 3.3.2**, the analysis found that the endometrium region was mainly composed of edge mask patterns. Analysis of the edge mask pattern was expanded to the frequencies of 16 edge mask patterns, as shown in Figure 3-9. In this analysis, angle information was defined for the 16 patterns. The ultrasonic images were rotated so that each uterus was positioned in a straight direction before analysis, because uterus directions in ultrasonic images were variable for each patient. Figure 3-10 shows an ultrasonic image before rotation. The arrow in Figure 3-10 shows the coordinate system after rotation. Uterine corpus and fundus directions were set as 90 degrees and 270 degrees, respectively. A vertical direction from the corpus to fundus was set as 0 and 180 degrees. This study analyzed the frequency of 16 patterns in 38 ultrasonic images.

Figure 3-11 shows a histogram of the 16 patterns. In Figure 3-11, the horizontal axis shows the angle and the vertical axis indicates the frequency for each angle pattern. Frequencies of angle patterns 0 degree and 180 degrees were higher than other patterns. Furthermore, there was a difference in the frequencies of 0 degree and 180 degrees patterns between patients exhibiting pregnancy and non-pregnancy. It was assumed that the smooth luminance gradient emerged from the center line of the endometrium in a vertical direction. The feature values f_1 and f_2 were defined considering this feature. f_1 and f_2 were calculated by equation (3-2) and (3-3), respectively.

$$f_1 = \sum h(157.5 \leq deg \leq 202.5)$$
$$+ \sum h(375.0 \leq deg) + \sum h(deg \leq 22.5) \tag{3-2}$$

$$f_2 = \frac{\sum h(157.5 \leq deg \leq 202.5)}{\sum h(375.0 \leq deg) + \sum h(deg \leq 22.5)} \tag{3-3}$$

32

mask pattern	1 1 1 / 1 _ 1 / 0 0 0	1 1 1 / 0 _ 1 / 0 0 0	1 1 1 / 0 _ 1 / 0 0 1	0 1 1 / 0 _ 1 / 0 0 1
angle [degree]	0.0	22.5	45.0	67.5
mask pattern	0 1 1 / 0 _ 1 / 0 1 1	0 0 1 / 0 _ 1 / 0 1 1	0 0 1 / 0 _ 1 / 1 1 1	0 0 0 / 0 _ 1 / 1 1 1
angle [degree]	90.0	112.5	135.0	157.5
mask pattern	0 0 0 / 1 _ 1 / 1 1 1	0 0 0 / 1 _ 0 / 1 1 1	1 0 0 / 1 _ 0 / 1 1 1	1 0 0 / 1 _ 0 / 1 1 0
angle [degree]	0.0	22.5	45.0	67.5
mask pattern	1 1 0 / 1 _ 0 / 1 1 0	1 1 0 / 1 _ 0 / 1 0 0	1 1 1 / 1 _ 0 / 1 0 0	1 1 1 / 1 _ 0 / 0 0 0
angle [degree]	270.0	292.5	315.0	337.5

Figure 3-9 Masks pattern and angles.
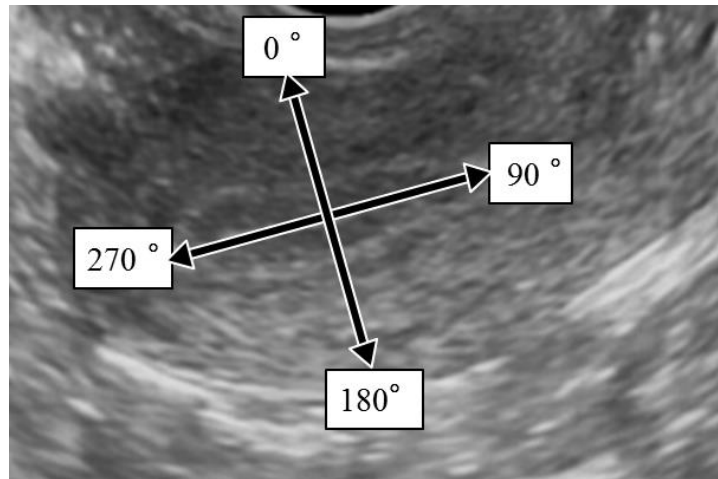
Figure 3-10 The coordinate system for the ultrasonic images.

The notation *deg* denotes angle information for mask patterns and *h* indicates the frequency. These feature values were calculated from a histogram of 16 edge mask patterns. Equation (3-2) shows the sum of the vertical direction (0 degree and 180 degree) frequency, and Equation (3-3) shows the ratio of the upward direction (0 degree) and the downward direction (180 degree) frequency. Figure 3-12 shows a graph plotting the feature values f_1 and f_2. In Figure 3-12, the vertical axis shows f_1 and the horizontal axis

indicates f_2. In Figure 3-12, points of LP, LN and HP are plotted at the front position, and points of HN are plotted at the back position relative to the other patterns. Therefore, it was assumed that the patients exhibiting homogeneous pattern showed different feature values between a pregnancy and non-pregnancy status.
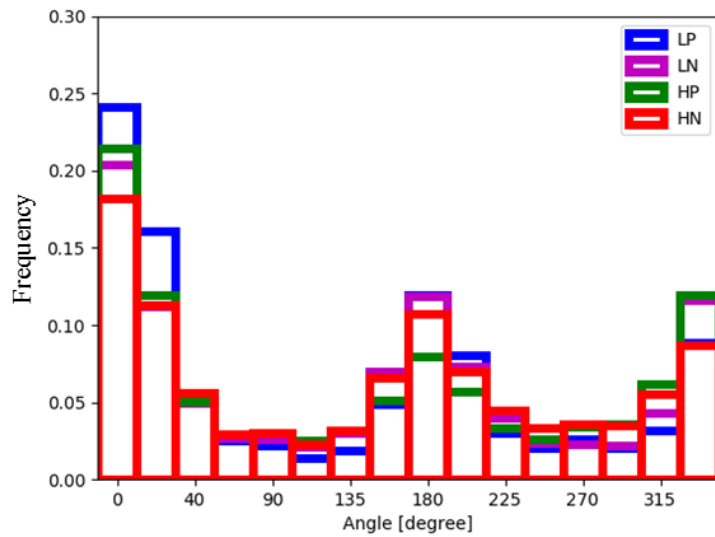
Figure 3-11 Histogram of the angles.

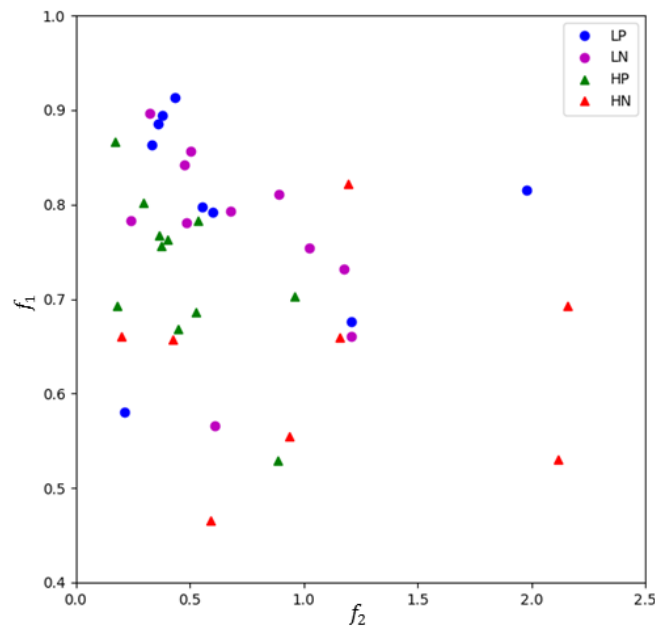L, leaf pattern. H, homogenous pattern. P, pregnancy. N, no pregnancy.

Figure 3-12 Plotted result for the feature values $f1$ and $f2$.

L, leaf pattern. H, homogenous pattern. P, pregnancy. N, no pregnancy.

3.3.4 Evaluation

This study analyzed whether it was possible to predict pregnancy or non-pregnancy outcomes using the feature values f_1 and f_2 of the ultrasonic images. A support vector machine (SVM) was used to predict pregnancy. A feature value of the SVM was two dimensional features f_1 and f_2. The feature value f_2 was normalized by Equation (3-4) before data was learned.

$$IF \ (1.0 \leq f_2) \qquad THEN \ (f_2 = 1.0) \qquad\qquad (3\text{-}4)$$

The learning data and test data used 38 ultrasonic images, as shown in Table 3-1 (19 pregnancy, 19 non-pregnancy). This prediction system was evaluated by leave-one-out cross-validation.

Table 3-3 shows the prediction results. The system had 0.68 accuracy. The prediction performance of the model was evaluated using distances of the samples to the separating hyperplane. Tables 3-4 and 3-5 show feature values obtained from these distances. The feature values were obtained by normalizing to scaling 0 and 1 after the distances were calculated. Tables 3-4 and 3-5 shows the feature values for pregnancy and non-pregnancy data, respectively. Figures 3-13 and 3-14 show a box plot and histogram for the feature values, respectively. There was no significant difference between feature values for pregnancy versus non-pregnancy, by a t-test for the feature values ($p = 0.508$). Figure 3-15 shows a receiver operating characteristic (ROC) curve for the feature values. In the ROC curve, the area under the curve (AUC) was 0.62, indicating that this model is not suitable.

3.3.5 Conclusion

In this section, a feature of uterine ultrasonic images was analyzed to develop a mechanical evaluation method to predict the success of pregnancy for female patients exhibiting infertility. The result survey using LBP_{ri} showed that a region of the endometrium was composed of an edge mask pattern. The current findings demonstrated that an angle feature of the edge mask pattern was different between the homogeneous pattern and pregnancy compared with the homogeneous pattern and non-pregnancy. The predictive rate of pregnancy by the angle feature system had 0.68 accuracy. However, the prediction results from the model found no significant difference between patients with pregnancy and non-pregnancy. It was assumed that to predict pregnancy from uterine shape was difficult because ultrasonic images of the uterine shape were not stable. Furthermore, the method was affected by uterine direction. Since uterine direction was manually aligned by rotating images, this method was subjective. Thus, it is difficult to develop an automated aligning uterine direction method, because of large individual variation in the shapes and sizes of endometrium. These issues present serious problems

for this proposed system.

Table 3-3 Predictive result (overall)

		Observation	
		Pregnancy (True)	No Pregnancy (False)
Forecast	Pregnancy (Positive)	15	8
	No Pregnancy (Negative)	4	11

Accuracy: 0.68

Table 3-4 Feature values for subjects with pregnancy.

Subject number	Feature value
1 (L)	0.75
2 (L)	0.71
3 (L)	0.52
4 (L)	0.66
5 (L)	0.47
6 (L)	0.73
7 (L)	0.80
8 (L)	0.04
9 (L)	0.07
10 (H)	0.69
11 (H)	0.09
12 (H)	1.00
13 (H)	0.66
14 (H)	0.70
15 (H)	0.59
16 (H)	0.11
17 (H)	0.53
18 (H)	0.78
19 (H)	0.52
AVG (SD)	0.55 (0.27)

Table 3-5 Feature values for subjects with no pregnancy.

Subject number	Feature value
1 (L)	0.12
2 (L)	0.70
3 (L)	0.26
4 (L)	0.92
5 (L)	0.88
6 (L)	0.08
7 (L)	0.45
8 (L)	0.47
9 (L)	0.11
10 (L)	0.67
11 (L)	0.68
12 (H)	0.15
13 (H)	0.45
14 (H)	0.94
15 (H)	0.00
16 (H)	0.68
17 (H)	0.11
18 (H)	0.09
19 (H)	0.08
AVG (SD)	0.41 (0.32)
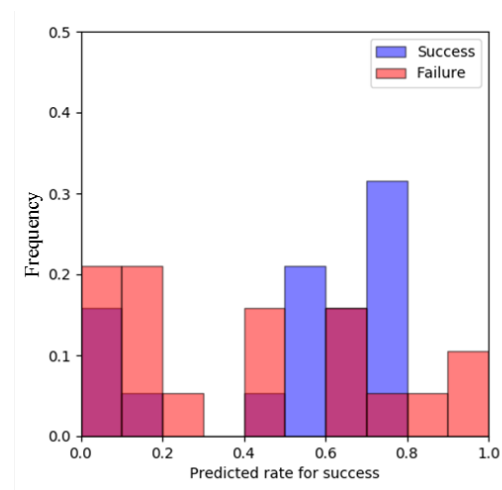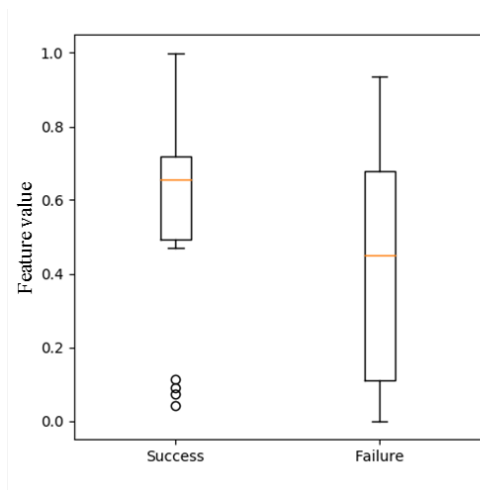
Figure 3-13 Box plot for the feature values.

Figure 3-14 Histogram for the feature values.

Success = pregnancy. Failure = no pregnancy.
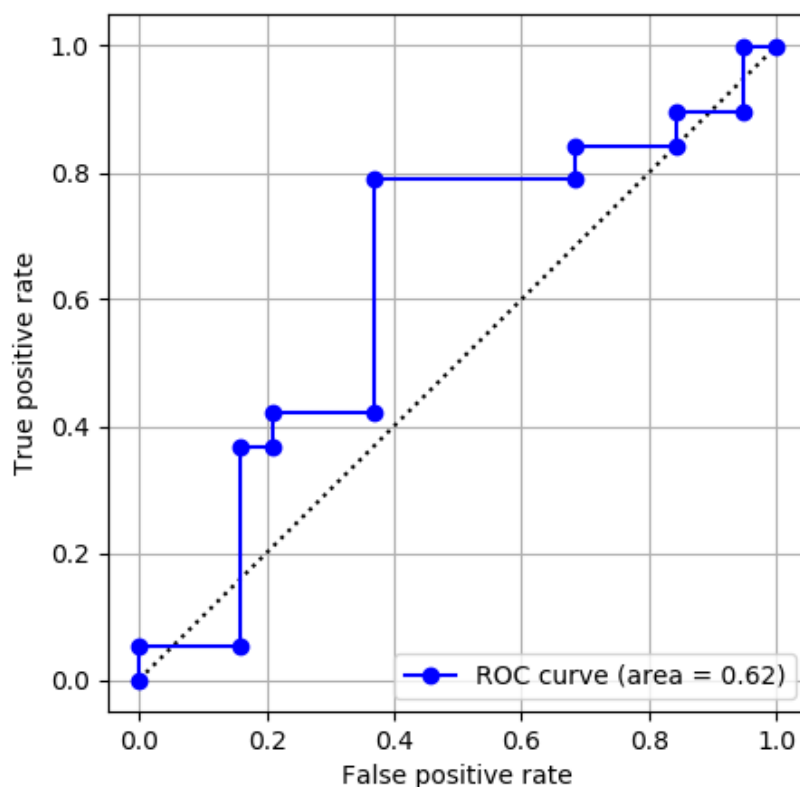
Figure 3-15 Receiver operating characteristic (ROC) curve.

3.4 Prediction Based on Velocity by CNN

In **Section 3.3**, the findings suggested that the proposed prediction system using LBP had problems. In this section, a prediction system for pregnancy without LBP was developed from a new viewpoint to solve these problems and improve prediction accuracy.

This section described a new prediction system composed of CNN using velocity information. An analysis method of this system was based on the analysis presented in **Chapter 2,** indicating that all uterine peristalsis exhibited a propagation constant velocity. In the current experiments, two CNN models were developed. One was composed of original ultrasonic images (conventional method using shape information) and other was a new method composed of images with velocity information (denoted a velocity-based system). The prediction accuracy for pregnancy was evaluated by comparative experiments.

3.4.1 Methods

This section details the two types of CNN approaches using shape- and velocity-based models. Figure 3-16 shows the structure of CNN models, which included a combination
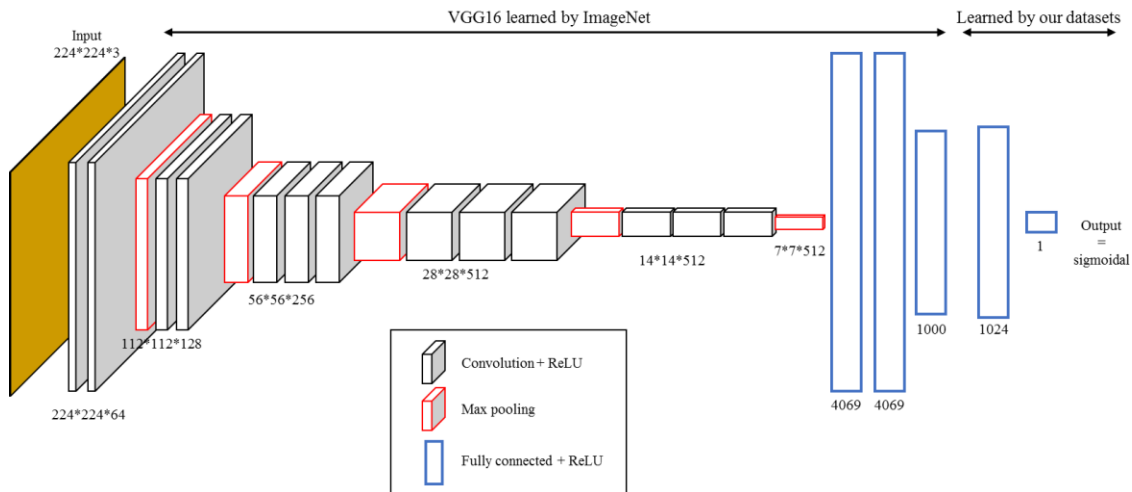
Figure 3-16 Convolution Neural Network (CNN) architecture.

of VGG16 [14] and fully connected layers. Because the VGG16 had been previously learned by ImageNet [25], the learning processes of these models was performed by transfer learning.

3.4.1.1 Shape-based Model

In this section, a shape-based system using CNN extracted endometrium shape information by convolution layers and then predicted pregnancy. It is generally thought that endometrial shapes can affect a pregnancy. Therefore, the system was defined as a conventional method.

Images were prepared as input for the CNN model. An averaging filter of 5×5 pixels was applied to ultrasonic images as preprocessing. An average image was generated every second from the movie file by calculating an average per time axis. Thirty images were generated from a 30-second movie by this process. An endometrial region was extracted from the average image by a mask image manually generated in advance. Figure 3-17 shows the original image, mask image, image extracted by the mask, and a resized image. The mask extracted endometrium regions from ultrasonic images. The considerable variation of endometrial shape and direction between individuals resulted in different extracted region sizes. Rotation processes every 60 degrees were applied to the extracted images. The obtained image was saved at 224×224 pixels. Figure 3-17 (d) shows a saved image at 224×224 pixels. Figure 3-18 shows an example of saved images. The vertical axis in Figure 3-18 shows the time of the movie file, and the horizontal axis shows the rotated images. Table 3-6 shows the number of saved images.

(a) Original image   (b) Mask image

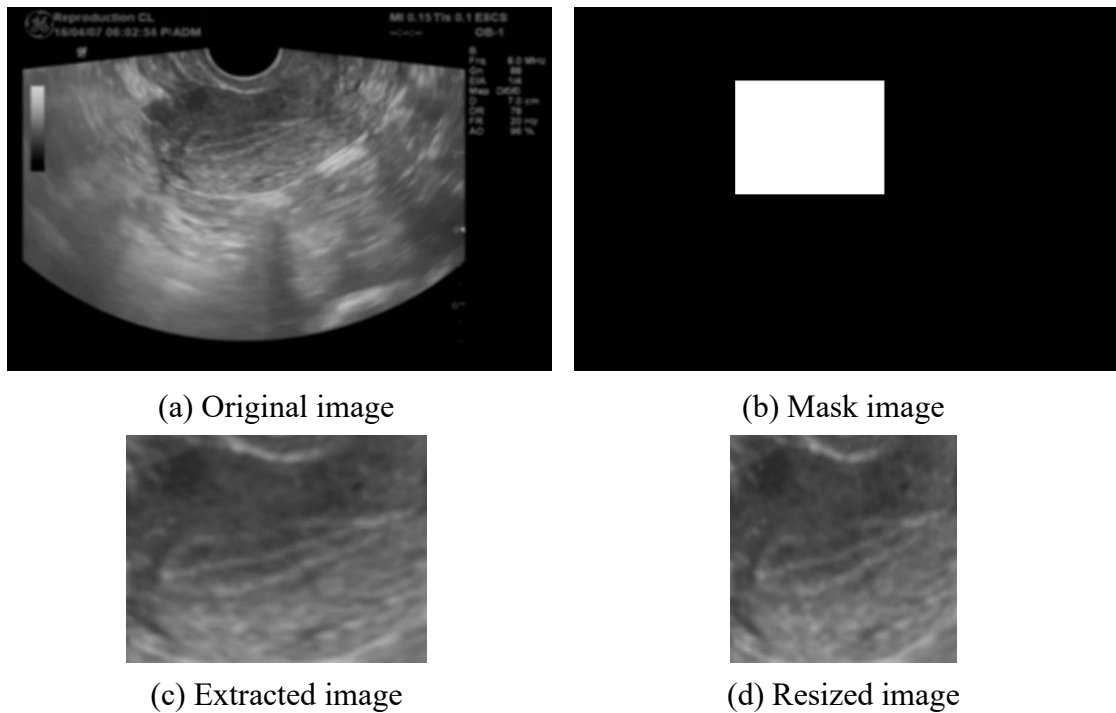(c) Extracted image   (d) Resized image

Figure 3-17 Examples of images in the mask process.

The learning process of CNN was performed using the saved images. Success or failure of pregnancy was predicted in the learned model. The system was evaluated by k-fold cross validation with $k = 3$. Images from 38 different patients were assigned to three groups. Table 3-7 shows the images divided into three groups. Subject's numbered 1 to 9 under pregnancy success and those numbered 1 to 11 under failure were all patients classified with an endometrium exhibiting a leaf pattern by physicians. Subject's numbered 10 to 19 under success and those numbered 12 to 19 under failure were patients classified as exhibiting endometrium with a homogenous pattern. The images from one group were extracted from the dataset as validation data, and the model used images from the remaining two groups as training data. Images that were not rotated in the validation data were used as test data. One patient had about 30 test images for a time series. The model performed learning analysis for 100 epochs. A pregnancy prediction for the test data was performed using the model after learning analysis for 100 epochs. The k-fold cross validation repeated learning while the groups were changed for validation data until all groups were used for validation data. Therefore, three learning curves and prediction results for the data from all patients were obtained. In the training and prediction process, labels of the images were set according to pregnancy success or failure for each patient. The images for subjects with successful pregnancy were labeled as success independent of time series. The images of subjects with no pregnancy were labeled as failure independent of time series.
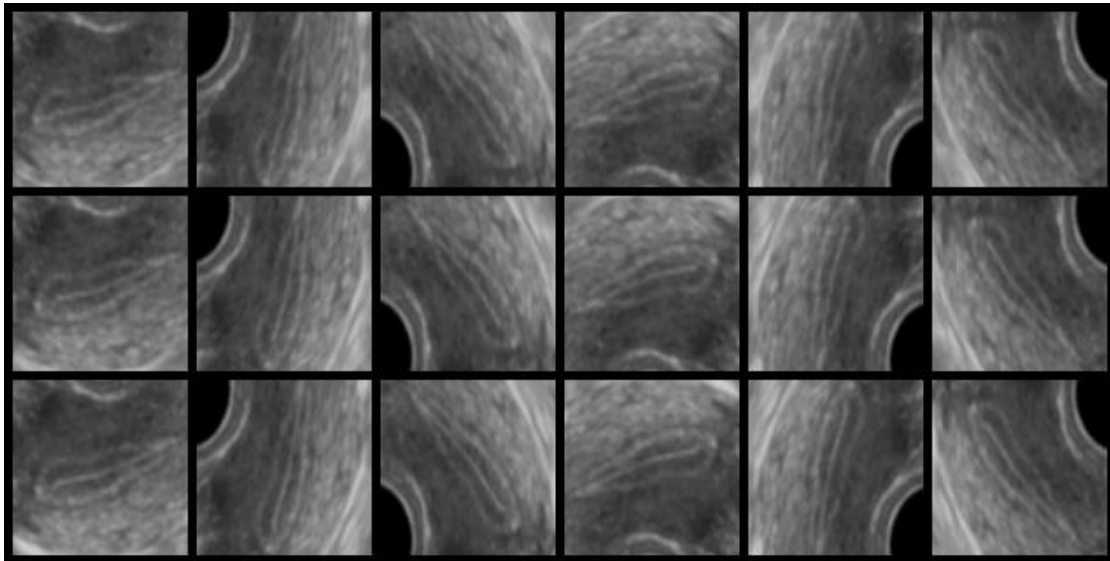
40

Figure 3-18 Examples of saved images.

Table 3-6 The number of saved images.

Success	3,432
Failure	3,408
Total	6,840

Table 3-7 The subjects for each group in the dataset.

	Group 1	Group 2	Group 3
Subject number with success	1, 2, 3, 10, 11, 12	4, 5, 6, 13, 14, 15	7, 8, 9 16, 17, 18, 19
Subject number with failure	1, 2, 3, 12, 13, 14	4, 5, 6, 7, 15, 16, 17, 18	8, 9, 10, 11, 18, 19
Number of images	2,190	2,316	2,334

3.4.1.2 Velocity-based Model

This section described a velocity-based prediction model using a CNN. This system predicted pregnancy by analyzing images with velocity information. A prediction method using velocity information has not been reported to date. Therefore, this system was defined as a proposed method.

Images were prepared as input for the CNN model. An averaging filter of 5×5 pixels was applied to ultrasonic images as preprocessing. An average image was generated every second from the movie files by calculating an average for the time axis. Thirty images were generated from a 30-second movie by this process. An endometrial

region was extracted from the average image by a mask image, as described in Section **3.4.1.1**. Because endometrial shape and direction exhibit variation between individuals, the size of extracted regions different from each other. Rotation processes every 60 degrees was applied to extracted images. Obtained images were saved as 224×224 pixels. The displacement D of each pixel was calculated as speed per second by applying an optical flow to saved images. A velocity image V was generated by normalizing D. Speed statistics for the dataset were calculated to set a standard of normalization. The speed information was calculated for images from 19 subjects with successful pregnancy. The fastest speed value in one image was recorded. A histogram for obtained speed values is shown Fig. 3-19. The average value of calculated speed was 0.78 mm/s with a standard deviation of 0.38 mm/s. The calculated average value was consistent with the 0.68 mm/s described in **Chapter 2**. A velocity image V was generated by normalizing D as shown in Equation (3-5).

If $|0.78 - D(x, y)| < 0.76$:

$$V(x, y) = \left(1 - \frac{|0.78 - D(x, y)|}{0.76}\right) \times 255 \tag{3-5}$$

Else:

$$V(x, y) = 0$$

The notations x and y denote the x and y coordinate points, respectively, in the image. Figure 3-20 shows an example of the velocity images. The vertical axis in Figure 3-20 shows the time of the movie file, and the horizontal axis shows rotated images.
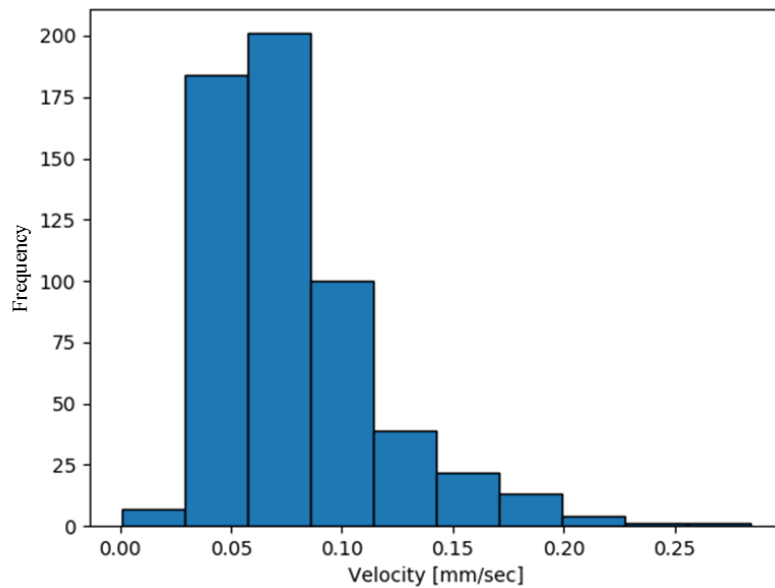
Figure 3-19 Histogram of the speed values.
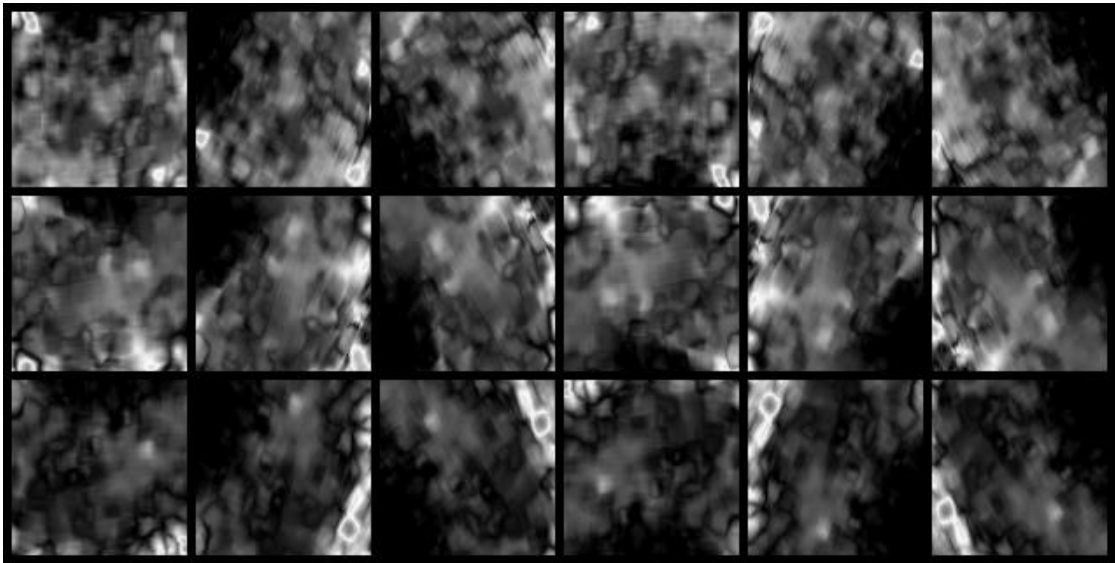
Figure 3-20 Examples of saved images.

3.4.2 Experimental Results

3.4.2.1 Shape-based Model

Figures 3-21 and 3-22 show the learning curves for accuracy and loss for each epoch, respectively. The solid and broken lines show average values of training and validation, respectively. The translucent region shows the maximum and minimum value range for the three learning curves. The accuracy was binary and the loss was binary cross entropy. The training accuracy increased with each epoch, but validation accuracy was not improved from around 0.56. Furthermore, training loss decreased with each epoch. Therefore, it is possible the overfitting occurred in the model.

The prediction accuracy for pregnancy was based on prediction rates for each patient. The prediction results for the test data were treated as time series data for each patient. Figure 3-23 shows examples of the time series data. Figures 3-23 (a) and (b) show the time series data of subject 4 (pregnancy success) and subject 6 (pregnancy failure), respectively. An average for this time series data was a feature value for the subject. Tables 3-8 and 3-9 show the feature values of the subjects labeled success and failure, respectively. Figures 3-24 and 3-25 show a box plot and a histogram for the feature values, respectively. Figures 3-24 and 3-25 show there was no significant difference in the feature values for pregnancy by t-test ($p = 0.092$). Figure 3-26 shows a ROC curve for the feature values, with the AUC = 0.65. This AUC value shows that the model was not suitable. If a cut off value was the left upper point in the ROC curve, the false positive rate, true positive rate, and threshold value were 0.37, 0.74, and 0.36, respectively. When the

threshold value was set at 0.36, the accuracy was 0.68. Table 3-10 shows a prediction result when the threshold value was set to 0.36.
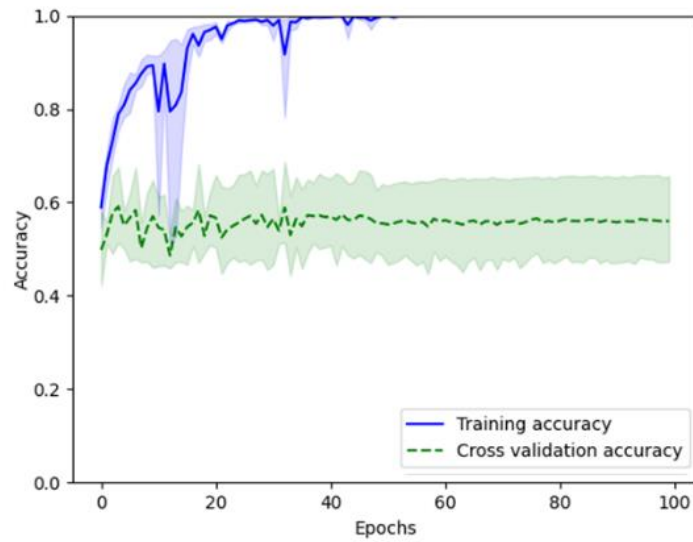

Figure 3-21 Learning curve showing cross-validation accuracy.
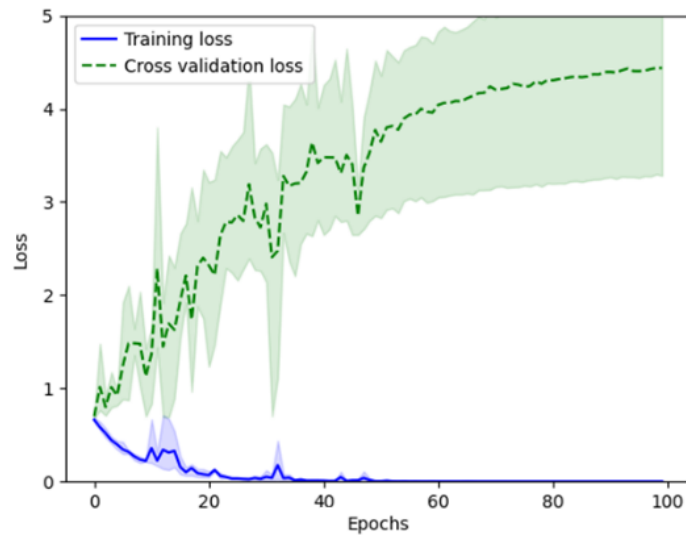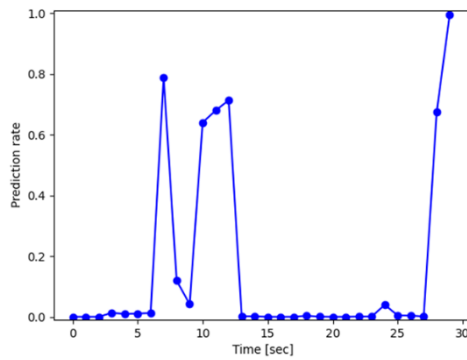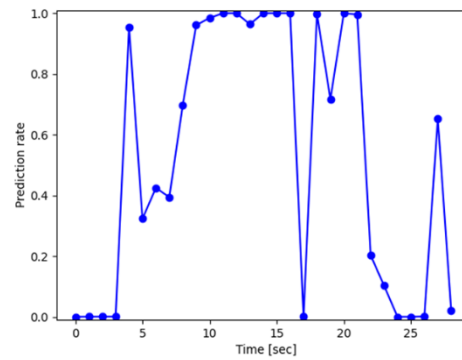

Figure 3-22 Learning curve showing cross-validation loss.

(a) Success, subject 4   (b) Failure, subject 6

Figure 3-23 Examples of time series prediction results.

Success = pregnancy. Failure = no pregnancy.

Table 3-8 Feature values for subjects with pregnancy (successful)

Subject number (L: *leaf*, H: *homogenous*) (validation group)	Feature value
1 (L) (1)	0.89
2 (L) (1)	0.51
3 (L) (1)	0.83
4 (L) (2)	0.16
5 (L) (2)	1.00
6 (L) (2)	0.09
7 (L) (3)	0.21
8 (L) (3)	0.00
9 (L) (3)	0.37
10 (H) (1)	0.59
11 (H) (1)	1.00
12 (H) (1)	0.96
13 (H) (2)	0.95
14 (H) (2)	1.00
15 (H) (2)	0.81
16 (H) (3)	0.00
17 (H) (3)	0.36
18 (H) (3)	0.52
19 (H) (3)	1.00
AVG (SD)	0.59 (0.36)

Table 3-9 Feature values for subjects with no pregnancy

Subject number (L: *leaf*, H: *homogenous*) (validation group)	Feature value
1 (L) (1)	1.00
2 (L) (1)	1.00
3 (L) (1)	0.00
4 (L) (2)	0.05
5 (L) (2)	0.27
6 (L) (2)	0.53
7 (L) (2)	0.01
8 (L) (3)	1.00
9 (L) (3)	0.00
10 (L) (3)	0.00
11 (L) (3)	0.27
12 (H) (1)	0.63
13 (H) (1)	0.14
14 (H) (1)	0.96
15 (H) (2)	0.97
16 (H) (2)	0.12
17 (H) (2)	0.03
18 (H) (3)	0.03
19 (H) (3)	0.05
AVG (SD)	0.37 (0.40)
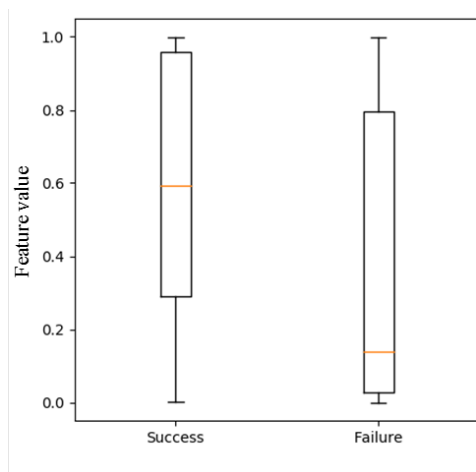
Figure 3-24 Box plot for the feature values.
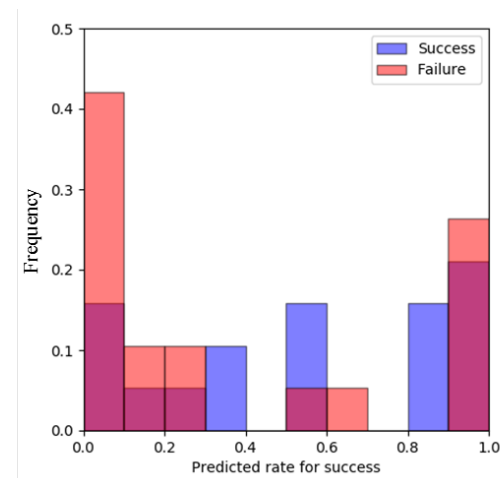
Figure 3-25 Histogram for the feature values.

Success = pregnancy. Failure = no pregnancy.
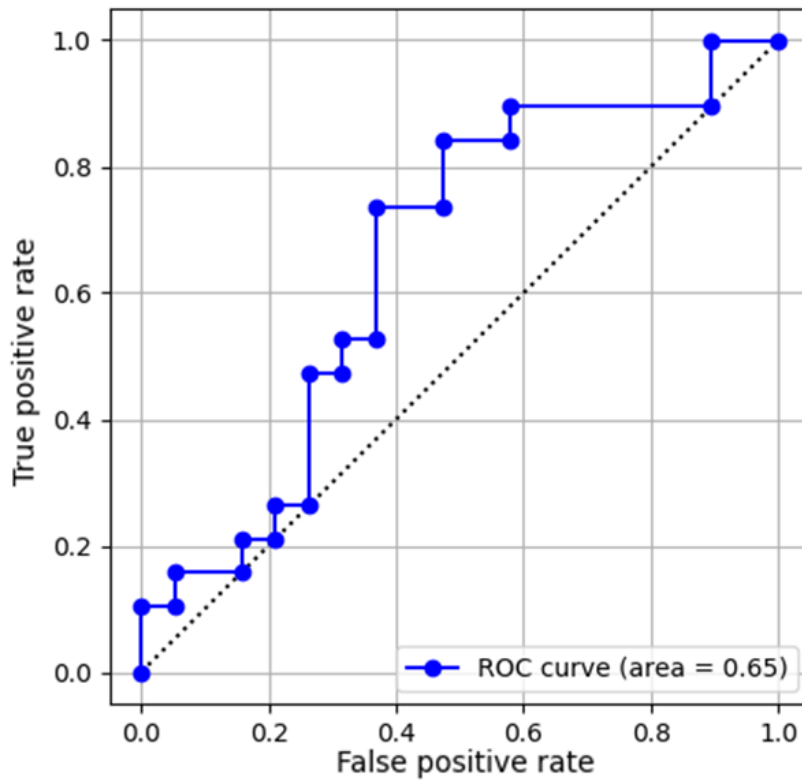
Figure 3-26 Receiver operating characteristic (ROC) curve.

Table 3-10 Prediction results of the conventional method using the threshold process

		Actual class	
		Success	Failure
Predicted class	Success	14	7
	Failure	5	12

Accuracy: 0.68

3.4.2.2 Velocity-based Model

Figures 3-27 and 3-28 show learning curves for the accuracy and loss for each epoch, respectively. The solid and broken lines show average values for the training and validation analysis, respectively. The shaded region shows the maximum and minimum value ranges for the three learning curves. The accuracy was binary and the loss was binary cross entropy. The training accuracy increased with the rising epoch, but the validation accuracy did not increase beyond approximately 0.61, as shown in Figure 3-27. Furthermore, training loss declined with increasing epochs. These results suggest that overfitting occurred in the model.

The prediction accuracy for pregnancy was based on a prediction rate for each patient. Prediction results for the test data were treated as time series data for each patient. Figure 3-29 shows examples of time series data. Figures 3-29 (a) and (b) show the time series data of subject 4 (pregnancy success) and subject 6 (pregnancy failure), respectively.

47

An average for this time series data was used as a feature value for the subject. Tables 3-11 and 3-12 show the feature values of the subjects with successful and failed pregnancy, respectively. Figures 3-30 and 3-31 show a box plot and a histogram for the feature values, respectively. Figures 3-30 and 3-31 show a significant difference in the feature values for pregnancy at the $p = 0.05$ level (since $p = 0.026$ from a t-test for the feature values). Figure 3-32 shows the ROC curve for these feature values, with the AUC = 0.72. If a cut off value was the left upper point of the ROC curve, the false positive rate, true positive rate, and threshold value were 0.37, 0.68, and 0.38, respectively. When the threshold value was set 0.38, the accuracy was 0.66, as shown in Table 3-13.
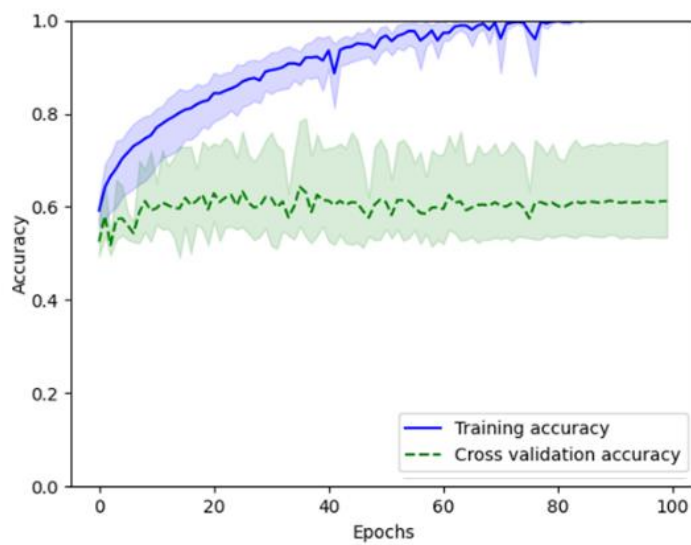
Figure 3-27 Learning curve showing cross-validation accuracy.
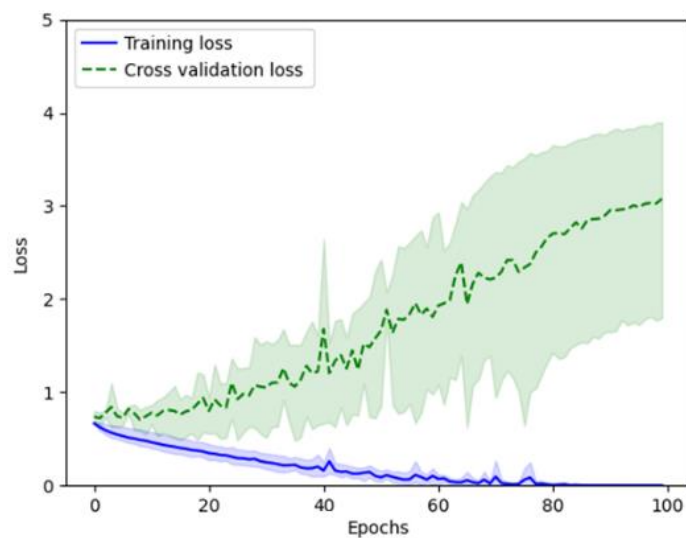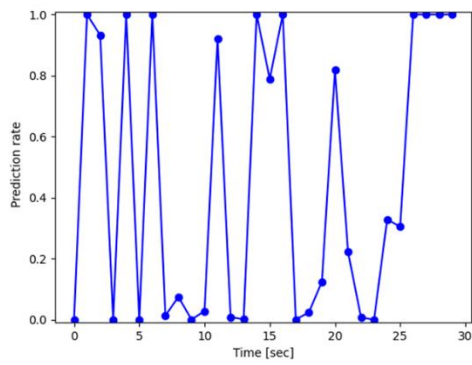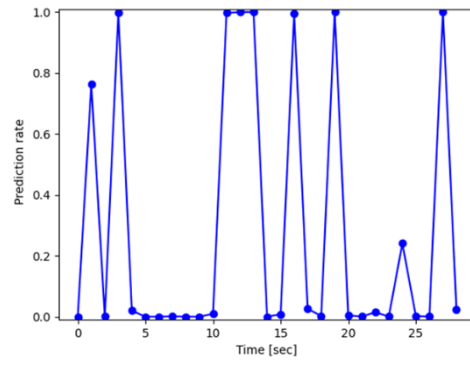

Figure 3-28 Learning curve showing cross-validation loss.

(a) Success, subject 4   (b) Failure, subject 6

Figure 3-29 Examples of time series prediction results.

Success = pregnancy. Failure = no pregnancy.

Table 3-11 Feature values for subjects with pregnancy (success).

Subject number (L: *leaf*, H: *homogenous*) (validation group)	Feature value
1 (L) (1)	0.92
2 (L) (1)	1.00
3 (L) (1)	0.32
4 (L) (2)	0.45
5 (L) (2)	1.00
6 (L) (2)	0.28
7 (L) (3)	0.34
8 (L) (3)	0.33
9 (L) (3)	0.08
10 (H) (1)	0.70
11 (H) (1)	0.50
12 (H) (1)	0.74
13 (H) (2)	0.38
14 (H) (2)	0.77
15 (H) (2)	0.52
16 (H) (3)	0.80
17 (H) (3)	0.47
18 (H) (3)	0.39
19 (H) (3)	0.35
AVG (SD)	0.54 (0.26)

Table 3-12 Feature values for subjects with no pregnancy (failure).

Subject number (L: *leaf*, H: *homogenous*) (validation group)	Feature value
1 (L) (1)	0.36
2 (L) (1)	0.07
3 (L) (1)	0.08
4 (L) (2)	0.37
5 (L) (2)	0.39
6 (L) (2)	0.28
7 (L) (2)	0.51
8 (L) (3)	0.26
9 (L) (3)	0.46
10 (L) (3)	0.73
11 (L) (3)	0.30
12 (H) (1)	0.24
13 (H) (1)	0.14
14 (H) (1)	0.45
15 (H) (2)	0.00
16 (H) (2)	1.00
17 (H) (2)	0.62
18 (H) (3)	0.29
19 (H) (3)	0.14
AVG (SD)	0.35 (0.24)
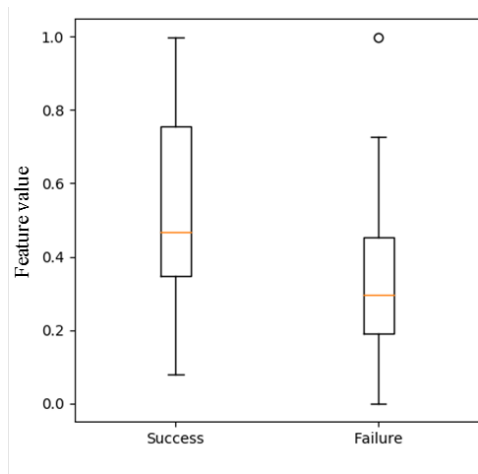
Figure 3-30 Box plot for the feature values.
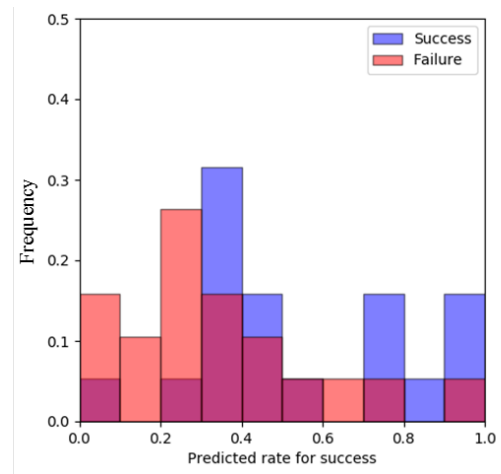
Figure 3-31 Histogram for the feature values.
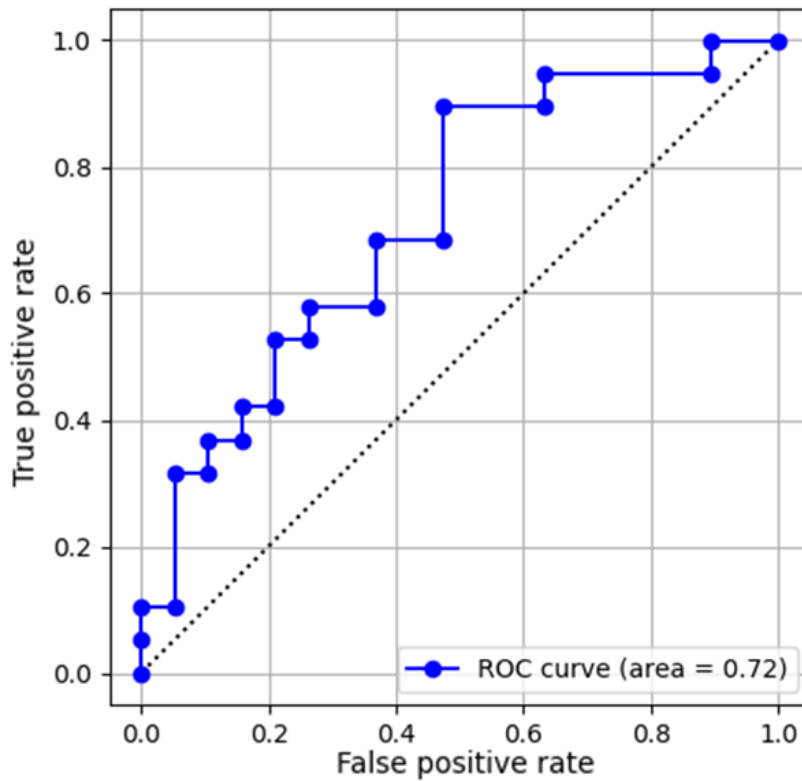
Success = pregnancy. Failure = no pregnancy.

Figure 3-32 Receiver operating characteristic (ROC) curve.

Table 3-13 Prediction results of the proposed using the threshold process

		Actual class	
		Success	Failure
Predicted class	Success	13	7
	Failure	6	12

Accuracy: 0.66

3.5 Comparison

Figure 3-33 compares the validation accuracy between the shape-based and velocity-based models, and Figure 3-34 compares the validation loss between the shape-based and velocity-based models. The validation accuracy for the velocity-based model was higher than in the shape-based model, and the validation loss was lower in the velocity-based model than the shape-based model. Therefore, the velocity-based model was more suitable than the shape-based model based on these results. Figure 3-35 compares the data in Figures 3-23 and 3-29. In Figure 3-35 (a), the prediction rate was higher for the velocity-based model compared with the shape-based model. In Figure 3-35 (b), the prediction rate was lower for the velocity-based model compared with the shape-based

model. The high prediction rate for pregnancy and low prediction rate for no pregnancy in the velocity-based model indicated that this model was more suitable than the shape-based model. Tables 3-14 and 3-15 compare the feature values by the LBP system, the shape-based, and velocity-based models. Figure 3-36 compares the ROC curves by the LBP system, the shape-based, and velocity-based models. In Figure 3-36, the AUC value from the velocity-based model was higher than other models, indicating that the velocity-based model is the most suitable model.
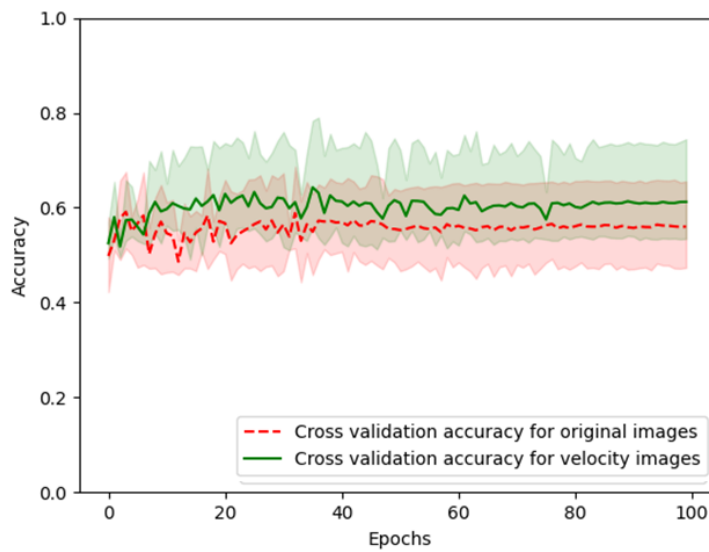
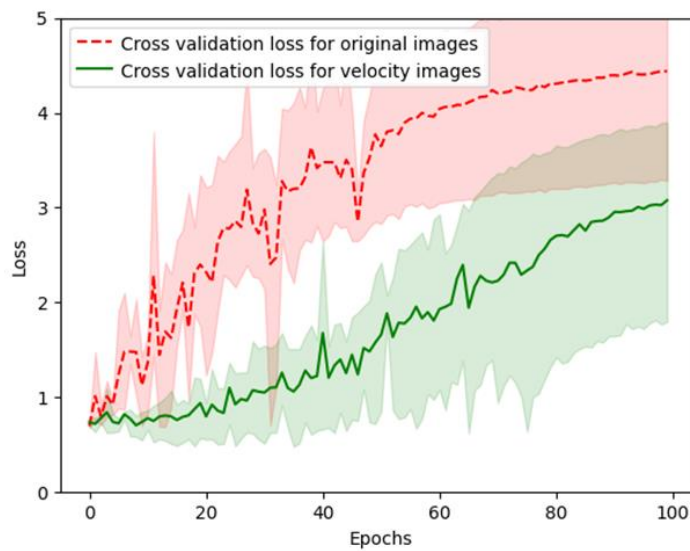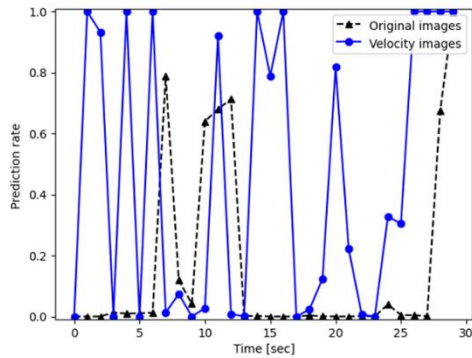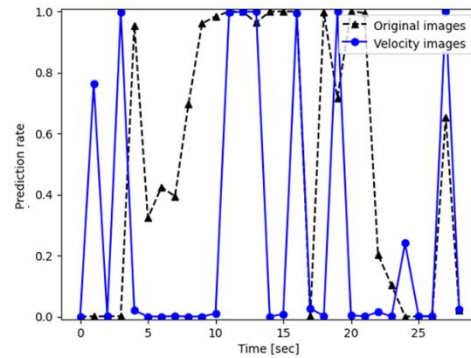Figure 3-33 Comparison of results for cross-validation accuracy.

Figure 3-34 Comparison of results for cross-validation loss.

(a) Success, subject 4   (b) Failure, subject 6

Figure 3-35 Comparison of the time series prediction results.

Success = pregnancy. Failure = no pregnancy.

Table 3-14 Feature values for subjects with pregnancy (success)

Subject number	Feature value		
	LBP system	Shape-based model	Velocity-based model
1 (L) (1)	0.75	0.89	0.92
2 (L) (1)	0.71	0.51	1.00
3 (L) (1)	0.52	0.83	0.32
4 (L) (2)	0.66	0.16	0.45
5 (L) (2)	0.47	1.00	1.00
6 (L) (2)	0.73	0.09	0.28
7 (L) (3)	0.80	0.21	0.34
8 (L) (3)	0.04	0.00	0.33
9 (L) (3)	0.07	0.37	0.08
10 (H) (1)	0.69	0.59	0.70
11 (H) (1)	0.09	1.00	0.50
12 (H) (1)	1.00	0.96	0.74
13 (H) (2)	0.66	0.95	0.38
14 (H) (2)	0.70	1.00	0.77
15 (H) (2)	0.59	0.81	0.52
16 (H) (3)	0.11	0.00	0.80
17 (H) (3)	0.53	0.36	0.47
18 (H) (3)	0.78	0.52	0.39
19 (H) (3)	0.52	1.00	0.35
AVG (SD)	0.55 (0.27)	0.59 (0.36)	0.54 (0.26)

Table 3-15 Feature values for subjects with no pregnancy (failure)

| Subject number	Feature value		
	LBP system	Shape-based model	Velocity-based model
1 (L) (1)	0.12	1.00	0.36
2 (L) (1)	0.70	1.00	0.07
3 (L) (1)	0.26	0.00	0.08
4 (L) (2)	0.92	0.05	0.37
5 (L) (2)	0.88	0.27	0.39
6 (L) (2)	0.08	0.53	0.28
7 (L) (2)	0.45	0.01	0.51
8 (L) (3)	0.47	1.00	0.26
9 (L) (3)	0.11	0.00	0.46
10 (L) (3)	0.67	0.00	0.73
11 (L) (3)	0.68	0.27	0.30
12 (H) (1)	0.15	0.63	0.24
13 (H) (1)	0.45	0.14	0.14
14 (H) (1)	0.94	0.96	0.45
15 (H) (2)	0.00	0.97	0.00
16 (H) (2)	0.68	0.12	1.00
17 (H) (2)	0.11	0.03	0.62
18 (H) (3)	0.09	0.03	0.29
19 (H) (3)	0.08	0.05	0.14
AVG (SD)	0.41 (0.32)	0.37 (0.40)	0.35 (0.24)
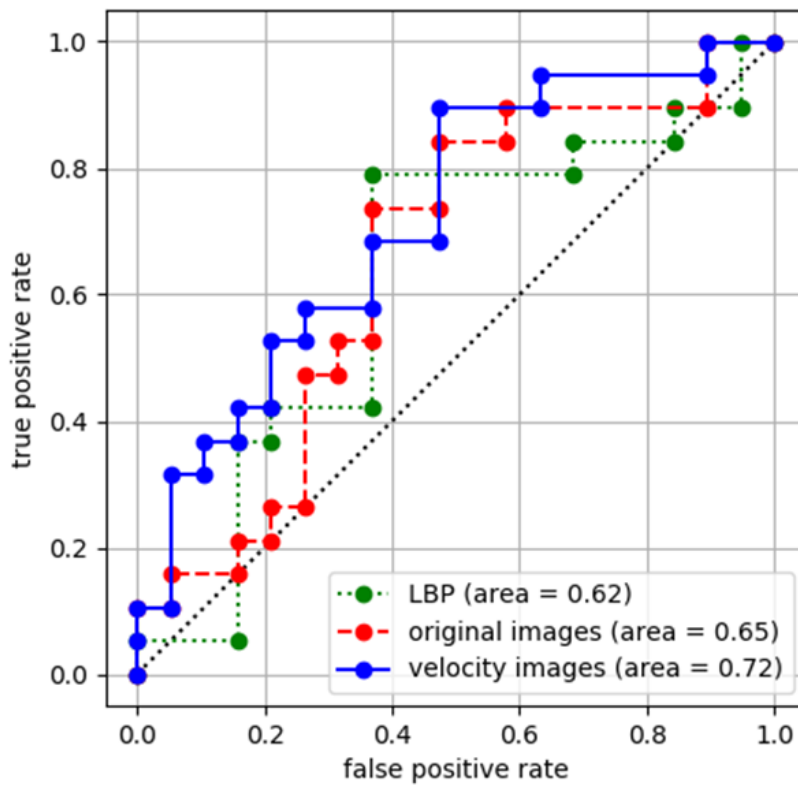
Figure 3-36 Comparison of the receiver operating characteristic (ROC) curves.

3.6 Conclusion

In this chapter, a system was developed to predict uterine ultrasonic B-mode images related to the success or failure of a pregnancy. This system predicts pregnancy based on uterine movement. Physicians typically determine endometrial shape to predict the optimal timing for fertility treatments to achieve predict pregnancy based on an endometrial shape. However, it is difficult to correctly evaluate endometrial shape by visual observation. The current system used information of endometrial movement as a new feature to predict pregnancy outcomes. Uterine movement is mainly analyzed using Cine MRI images because these images can be analyzed more easily than ultrasonic images. Uterine movement affects pregnancy. However, prediction models using a feature of uterine movement has not been reported for ultrasonic images. In this thesis it was proposed that it is possible to analyze uterine movements from ultrasonic images by extracting the movement with a constant speed. Findings obtained from the analysis of Cine MRI images was applied to investigate ultrasonic images and develop a new system. Because the knowledge of uterine movement obtained from the analysis of Cine MRI images can be applied to the analysis of ultrasonic images, it was predicted that the

success rate of fertility treatment will increase. The direction and frequency of uterine peristalsis change in each phase of the menstrual cycle. We demonstrated that a uterus suitable for a successful pregnancy has uterine peristalsis, and a uterus unsuitable for pregnancy does not have uterine peristalsis. The system predicted the success or failure of a pregnancy with an AUC of 0.72, which was higher than a system using endometrial shape information.

Chapter 4
Conclusions

The number of people treated for infertility is increasing annually, but the success rate is not improving. The success rate of ART is higher than that of conventional fertility treatment methods, but the success rate remains low. Currently, there is limited opportunity for artificial intervention during the embryo transfer step of ART, so new techniques are required to improve the success rate. One problem for ART is that the clinically defined uterine characteristics for pregnancy have not been clarified. Uterine peristalsis assists in the transport of sperm. The direction and frequency of uterine peristalsis are known to change in each phase of the menstrual cycle; however, random and mixed movements occur in all phases of the menstrual cycle in infertile patients. These random and mixed movements had not been analyzed in detail. This thesis analyzed uterine movements using Cine MRI images from patients with infertility. This analysis identified six fundamental movement patterns in Cine MRI images, by visual inspection, from the infertile patients. Visual simulation mimicked the movements defined from original Cine MRI images, and supported the classification of these uterine movements. The simulation model revealed that all uterine peristalsis exhibited a constant propagation velocity of 0.68 mm/s. Using this velocity feature, a CNN system was developed that predicts uterine movement patterns. Comparative analysis was used to compare the original MRI images with velocity images generated from the velocity feature. In sagittal plane images, the prediction accuracy of the velocity image system was higher than that of the original image system. However, in transverse plane images, the prediction accuracy of the velocity image system was not improved compared with the original MRI image system. The difference between sagittal and transverse images may be caused by the lack of distance per pixel information. Furthermore, it is possible that the model had insufficient learning analysis, because individual variations of endometrial shape and size were larger in transverse plane images than in sagittal plane images.

The current research then developed a system to predict pregnancy outcomes

from ultrasonic images. In fertility treatment, physicians decide the timing of embryo transfer by analyzing endometrium shape on ultrasonic B-mode images. However, the treatment sometimes fails when physicians define a suitable endometrial shape, and treatment may succeed when physicians define an unsuitable endometrial shape. It is difficult to correctly evaluate endometrium shape by a visual inspection. To solve the problem of determining the optimal uterine feature for the timing of embryo transfer leading to a successful pregnancy, we developed a prediction system using LBP. This system predicted a pregnancy outcome based on endometrial shape with 0.68 accuracy. The model was evaluated by ROC curve analysis; however, the AUC of 0.62 indicated the system was not a suitable prediction model. The current research developed a new prediction system using the velocity feature (uterine peristalsis has a constant velocity of 0.68 mm/s) obtained from Cine MRI analysis. The new system was composed of a CNN, and was evaluated using experiments comparing original images and velocity images generated from the velocity feature. This analysis produced prediction accuracies of 0.68 and 0.66 for the original and velocity image systems, respectively. The accuracy of the velocity image system was lower than the LBP and original image systems. The models were evaluated by ROC curve analysis, which produced obtained AUC of 0.65 and 0.72 for the original and velocity image systems, respectively. These findings demonstrated that the velocity image system provides a good model, because the AUC was higher with the velocity image system compared with the other systems, including the LBP system.

This study revealed that all uterine peristalsis displayed at a constant propagation velocity. This novel velocity feature was applied to pregnancy outcome prediction from uterine analysis. In clinical image analysis for infertility, it is very important to analyze uterine movement because uterine movement and infertility are closely related. To date, it has been difficult to analyze uterine movement by image analysis. The large variation in endometrial shape and size between individuals, presented a challenge to generating a generalized prediction model. The new velocity feature overcomes these problems and is expected to contribute to the growth of related studies.

In the current study, the movement prediction system for Cine MRI images showed no improvement using the velocity images. However, the new pregnancy prediction system for ultrasonic images was improved by the velocity images. It is predicted that these findings reflect information about the distance per pixel. In the dataset of ultrasonic images, memory of the actual size was retrieved in the images. However, information to determine the relationship between pixels and distance was lacking in the dataset of Cine MRI images. Such information is needed to perform analysis based on the velocity. In previous studies, this information was not viewed as important. In the future, this information should be gathered to allow the application of the proposed new method.

In the current field of clinical image analysis, it is difficult to collect datasets that could be used in the current studies. There were not enough images to use a CNN in the current system, and the learning curves showed a tendency for overfitting. To avoid overfitting, it will be necessary to increase the number of collected images in future research. In recent years, data expansion by generative adversarial networks (GANs) [39, 40, 41, 42, 43, and 44] has been attracting attention. The application of GANs has been reported in the field of medical imaging research [45, 46, 47, 48, 49, 50, and 51]. Future work should develop data augmentation methods for medical images to improve the accuracy of the new prediction system.

Acknowledgments

First and foremost, I would like to express my sincerest gratitude to my supervisor Professor Yutaka Hata of the University of Hyogo, for the continuous support and instilled mental stimulation during my Ph.D. candidature, with his motivation and immense knowledge. I also thank to Doctor Tadahiko Murata of the Kansai University, Doctor Yoshi Fujiwara, and Doctor Shugo Yasuda of the University of Hyogo for providing lucid and valuable insights throughout my work.

I firmly believe that my research would not have been completed without valuable medical advice and support. I would like to thank Doctor Yoshimitsu Tokunaga, Doctor Tetsurou Sakumoto, Doctor Akira Nashima, and Doctor Isamu Komesu of the SORA no MORI CLINIC, and Doctor Kotaro Kitaya, Doctor Tomomoto Ishikawa, and Doctor Hidehiko Matsubayashi of the Reproduction Clinic.

Special thanks are due to Doctor Hiroshi Nakajima, Doctor Yasuyo Kotake and Ms. Danni Wang of the Omron Corporation, Doctor Syoji Kobashi of the University of Hyogo, Doctor Naomi Yagi of the Himeji Dokkyo University, Mr. Toshiyuki Sawayama and Mr. Takuya Sawayama of the New Sensor Incorporated, Doctor Atsushi Kono of the National Cerebral and Cardiovascular Center, Doctor Patrick Chan of the South China University of Technology, Ms. Satomi Ihara of University of Hyogo, Doctor Shigeyasu Nakagawa, Doctor Hideaki Katayama, Doctor Atsushi Utsumi, Doctor Keita Ashizawa, Doctor Hidetake Funaki, Doctor Yutaka Tange, Doctor Yasuhito Inoue, Doctor Nobuya Hiroshiba, and Doctor Kimihiro Nanamori of the National Institute of Technology, Maizuru College. They inspired me to take pride in my research; their enthusiasm for research efforts will have a significant effect on my future projects. Their heartfelt encouragement with consistent quality contributed to my growth as a scientist.

In addition, I am very grateful to the Tateishi Science and Technology Foundation for providing me a research grant. I also sincerely thank all laboratory members of the University of Hyogo for supporting every phase of this work.

I would like to thank Bentham science, Current Medical Imaging for pu blishing my article "A Uterine Motion Classification in MRI data for Female Inf ertility". The published manuscript is available at EurekaSelect via http://www.eur ekaselect.com/openurl/content.php?genre=article&doi=10.2174/1573405614666180917 123654.

Last but not least, I owe eternal thanks to everyone who has supported me academically and spiritually throughout my research life.

References

[1] WHO | Infertility definitions and terminology (Aug. 27, 2020)
https://www.who.int/reproductivehealth/topics/infertility/definitions/en/

[2] ART データブック 2017 (Aug. 27, 2020)
https://plaza.umin.ac.jp/~jsog-art/

[3] Centers for Disease Control and Prevention. 2017 Assisted Reproductive Technology Fertility Clinic Success Rates Report.
Retrieved from https://www.cdc.gov/art/artdata/index.html

[4] R. Kashiwaki, T. Ishikawa, H. Matsubayashi, and Y. Hata, "Classification of Follicles by Ultrasonic Images", Proc. of the 2018 IEEE International Conference on Systems, Man, and Cybernetics (SMC2018), pp.368-371, 2018.

[5] Y. Kinishi, T. Maekawa, S. Mizuta, T. Ishikawa, and Y. Hata, "Detection of Optimal Puncture Position in Ovum Images for Artificial Insemination", Proc.of the International Conference on Machine Learning and Cybernetics, pp.140-144, 2019.

[6] K. d. Vries, E. A. Lyons, G. Ballard, C.S. Levi, and D.J. Lindsay, "Contractions of the inner third of myometrium", American Journal of Obstetrics Gynecology, Vol. 162, No. 3, pp. 679-682, 1990.

[7] E. A. Lyons, P. J. Taylor, X. H. Zheng, G. Ballard, C. S. Levi, and J. V. Kredentser, "Characterization of subendometrial myometrial contractions throughout the menstrual cycle in normal fertile women", Fertility and Sterility Vol. 55, No. 4, pp. 771-774, 1991.

[8] G. Kunz, D. Beil, H. Deininger, L. Wildt, and G. Leyendecker, "The dynamics of rapid sperm transport through the female genital tract: evidence from vaginal sonography of uterine peristalsis and hysterosalpingoscintigraphy", Human Reproduction Vol. 11, No. 3, pp. 627-632, 1996.

[9] A. Nakai, K. Togashi, T. Yamaoka, T. Yamaoka, T. Fujiwara, H. Ueda, T. Koyama, H. Kobayashi, T. Kagimura, S. Fujii and J. Konishi, "Uterine Peristalsis Shown on Cine MR Imaging Using Ultrafast Sequence", Journal of Magnetic Resonance Imaging, Vol. 18, No. 6, pp. 726-733, 2003.

[10] A. C. Fleischer, D. E. Pittaway, L. A. Beard, G. A. Thieme, A. L. Bundy, A. E. James Jr, and A. C. Wentz, "Sonographic Depiction of Endometrial Changes Occurring with Ovulation Induction", Journal of Ultrasound in Medicine, Vol. 3, No. 8, pp. 341-346, 1984.

[11] A. C. Fleischer, C. M. Herbert, G. A. Sacks, A. C. Wentz, S. S. Entman, and A. E. James Jr, "Sonography of the endometrium during conception and nonconception cycles of in vitro fertilization and embryo transfer", Fertility and Sterility, Vol. 46,

No. 3, pp. 442-447, 1986.

[12] T. S. Forrest, M. K. Elyaderani, M. I. Muilenburg, C. Bewtra, W. T. Kable, and P. Sullivan, "Cyclic endometrial changes: US assessment with histologic correlation", Radiology, Vol. 167, No. 1, pp. 233-237, 1988.

[13] A. Krizhevsky, I. Sutskever, and G. E. Hinton, "ImageNet Classification with Deep Convolutional Neural Networks", Proc. of the 25th International Conference on Neural Information Processing Systems, pp. 1097-1105, 2012.

[14] K. Simonyan and A. Zisserman, "Very Deep Convolutional Networks for Large-Scale Image Recognition", Proc. of the International Conference on Learning Representations, 2015.

[15] K. He, X. Zhang, S. Ren, and J. Sun, "Deep Residual Learning for Image Recognition", Proc. of the IEEE Conference on Computer Vision and Pattern Recognition, 2016.

[16] M. Anthimopoulos, S. Christodoulidis, L. Ebner, A. Christe, and S. Mougiakakou, "Lung Pattern Classification for Interstitial Lung Diseases Using a Deep Convolutional Neural Network", IEEE Transactions on Medical Imaging, Vol. 35, No. 5, pp. 1207-1216, 2016.

[17] M. H. Yap, G. Pons, J. Marti, S. Ganau, M. Sentis, R. Zwiggelaar, A. K. Davison, and R. Marti, "Automated Breast Ultrasound Lesions Detection Using Convolutional Neural Networks", IEEE Journal of Biomedical and Health Informatics, Vol. 22, No. 4, pp. 1218-1226, 2018.

[18] G. Liang, H. Hong, W. Xie, and L. Zheng, "Combining Convolutional Neural Network With Recursive Neural Network for Blood Cell Image Classification", IEEE Access, Vol. 6, pp. 36188-36197, 2018.

[19] A. Yang, X. Yang, W. Wu, H. Liu, and Y. Zhuansun, "Research on Feature Extraction of Tumor Image Based on Convolutional Neural Network", IEEE Access, Vol. 7, pp. 24204-24213, 2019.

[20] K. Mori, Y. Tokunaga, T. Sakumoto, A. Nakashima, I. Komesu, and Y. Hata, "A Uterine Motion Classification in MRI data for Female Infertility", Bentham science, Current Medical Imaging, Vol. 16, No. 5, pp. 479 – 490, 2020.

[21] K. Mori, K. Kitaya, T. Ishikawa, and Y. Hata, "Analysis of Endometrium Form by Using LBP for Female Infertility", Proc. of the International Conference on Machine Learning and Cybernetics, 2018.

[22] K. Mori, K. Kitaya, T. Ishikawa, and Y. Hata, "A Pregnancy Prediction System based on Uterine Peristalsis from Ultrasonic Images", Intelligent Automation and Soft Computing Journal, 2020. [in press]

[23] A. Kido, M. Nishiura, K. Togashi, A. Nakai, T. Fujiwara, M. L. Kataoka, T. Koyama,

S. Fujii, N. Asada, "A semiautomated technique for evaluation of uterine peristalsis" Journal of Magnetic Resonance Imaging, Vol. 21, No. 3, pp. 249-57, 2005.

[24] K. Yee, "Numerical solution of initial boundary value problems involving maxwell's equations in isotropic media", IEEE Transactions on Antennas and Propagation, Vol. 14, No. 3, pp. 302-307, 1996.

[25] Visual Geometry Group - University of Oxford (Accesed 10. 9. 2020) http://www.robots.ox.ac.uk/~vgg/research/very_deep/

[26] G. Farneback, "Two-Frame Motion Estimation Based on Polynomial Expansion." Proc. of the 13th Scandinavian Conference on Image Analysis, pp. 363 - 370, 2003.

[27] T. Ojala, M. Pietikainen, and D. Harwood, "Performance evaluation of texture measures with classification based on Kullback discrimination of distributions", Proc. of the 12th International Conference on Pattern Recognition, pp. 582-585, 1994.

[28] T. Ojala, M. Pietikainen, and D. Harwood, "A Comparative Study of Texture Measures with Classification Based on Feature Distributions", Pattern Recognition, Vol. 29, No. 1, pp. 51-59, 1996.

[29] B. Yang, and S. Chen, "A comparative study on local binary pattern (LBP) based face recognition: LBP histogram versus LBPimage", Neurocomputing, Vol. 120, No. 23, p. 365-379, 2013.

[30] R. Nosaka, Y. Ohkawa, and K. Fukui, "Feature Extraction Based on Co-occurrence of Adjacent Local Binary Patterns", Proc. of the Advances in Image and Video Technology, pp. 82-91, 2011.

[31] L. Zhang, R. Chu, S. Xiang, S. Liao, and S. Z. Li, "Face Detection Based on Multi-Block LBP Representation", Proc. of the International Conference on Advances in Biometrics, pp. 11-18, 2007.

[32] X. Tan, and B. Triggs, "Fusing Gabor and LBP Feature Sets for Kernel-based Face Recognition", Proc. of the 3rd International Conference on Analysis and Modeling of Faces and Gestures, pp. 235-249, 2007.

[33] Z. Camlica, H. R. Tizhoosh, and F. Khalvati, "Medical Image Classification via SVM using LBP Features from Saliency-Based Folded Data", Proc. in the International Conference on Machine Learning and Applications, 2015.

[34] G. Tian, H. Fu, and D. D. Feng, "Automatic Medical Image Categorization and Annotation Using LBP and MPEG-7 Edge Histograms", Proc. of the International Conference on Information Technology Applications in Biomedicine, 2008.

[35] T. J. Alhindi, S. Kalra, K. H. Ng, A. Afrin, and H.R. Tizhoosh, "Comparing LBP, HOG and Deep Features for Classification of Histopathology Images", Proc. of the International Joint Conference on Neural Networks, 2018.

[36] D. Unay, A. Ekin, M. Cetin, R. Jasinschi, and A. Ercil, "Robustness of Local Binary Patterns in Brain MR Image Analysis", Proc. of the Annual International Conference of the IEEE Engineering in Medicine and Biology Society, 2007.

[37] L. Nanni, A. Lumini, and S. Brahnam, "Local binary patterns variants as texture descriptors for medical image analysis", Artificial Intelligence in Medicine, Vol. 49, No. 2, pp. 117-125, 2010.

[38] M. Nishiura, M. Yuasa and M. Watanabe, "Active contour extraction method using partial shape constraint contour model", Systems and Computers in japan, Vol. 31, No. 14, pp. 20-28, 2000.

[39] I. J. Goodfellow, J. P. Abadie, M. Mirza, B. Xu, D. W. Farley, S. Ozair, A. Courville, and Y. Bengio, "Generative Adversarial Nets", Proc. of the Advances in Neural Information Processing Systems 27, 2014.

[40] A. Radford, L. Metz, and S. Chintala, "Unsupervised Representation Learning with Deep Convolutional Generative Adversarial Networks", Proc. of the International Conference on Learning Representations, 2016.

[41] A. Odena, C. Olah, J. Shlens, "Conditional Image Synthesis With Auxiliary Classifier GANs", Proc. of the 34th International Conference on Machine Learning, 2017.

[42] A. Shrivastava, T. Pfister, O. Tuzel, J. Susskind, W. Wang, R. Webb, "Learning from Simulated and Unsupervised Images through Adversarial Training". Proc of the IEEE Conference on Computer Vision and Pattern Recognition, pp. 2107-2116, 2017.

[43] T. Karras, T. Aila, S. Laine, J. Lehtinen, "Progressive Growing of GANs for Improved Quality, Stability, and Variation", Proc. of the International Conference on Learning Representations, 2018.

[44] H. Zhang, I. Goodfellow, D. Metaxas, A. Odena, "Self-Attention Generative Adversarial Networks", Proc. of the 36th International Conference on Machine Learning, 2019.

[45] M. F. Adar, E. Klang, M. Amitai, J. Goldberger, H. Greenspan, "Synthetic Data Augmentation using GAN for Improved Liver Lesion Classification", Proc. of the International Symposium on Biomedical Imaging, 2018.

[46] T. Schlegl, P. Seeböck, S. M. Waldstein, U. S. Erfurth, G. Langs, "Unsupervised Anomaly Detection with Generative Adversarial Networks to Guide Marker Discovery", Proc. of the International Conference on Information Processing in Medical Imaging, pp. 146-157, 2017.

[47] M. F. Adar, I. Diamant, E. Klang, M. Amitai, J. Goldberger, and H. Greenspan, "GAN-based synthetic medical image augmentation for increased CNN

performance in liver lesion classification", Neurocomputing, Vol. 321, No. 10, pp. 321-331, 2018.

[48] T. Iqbal and H. Ali, "Generative Adversarial Network for Medical Images (MI-GAN)", Journal of Medical Systems, Vol. 42, No. 231, 2018.

[49] Y. Mirsky, T. Mahler, I. Shelef, and Y. Elovici, "CT-GAN: Malicious Tampering of 3D Medical Imagery using Deep Learning", Proc. of the USENIX Security Symposium, 2019.

[50] J. Zhu, G. Yang, and P. Lio, "How Can We Make Gan Perform Better in Single Medical Image Super-Resolution? A Lesion Focused Multi-Scale Approach", Proc. of the International Symposium on Biomedical Imaging, 2019.

[51] X. Yi, E. Walia, and P. Babyn, "Generative Adversarial Network in Medical Imaging: A Review", Medical Image Analysis, Vol. 58, 2019.

Appendix

The captured images for the MRI and simulation results for every 5 frames are shown in Figures A-1 to 18. Images on the left show that the simulation results overlapped with the MRI images. In the simulation results, images were tilted −15 degrees, black and red in the images were replaced with a transparent color, and the alpha value was decreased to 20%. Images on the right show the simulation results. These images are snap shots of the movie file with 3 seconds (90 frames).
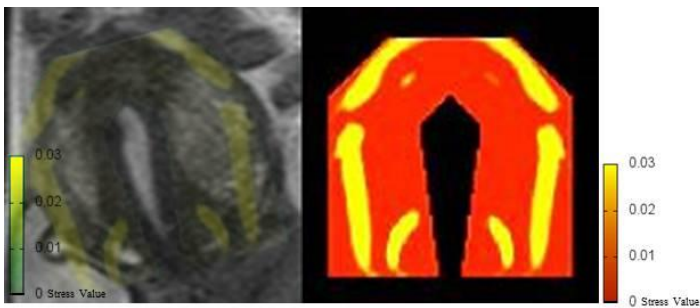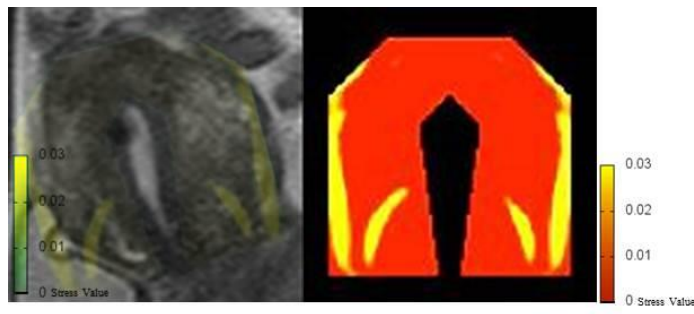

Figure A-1 Comparing MRI and simulation (0/90) [20].

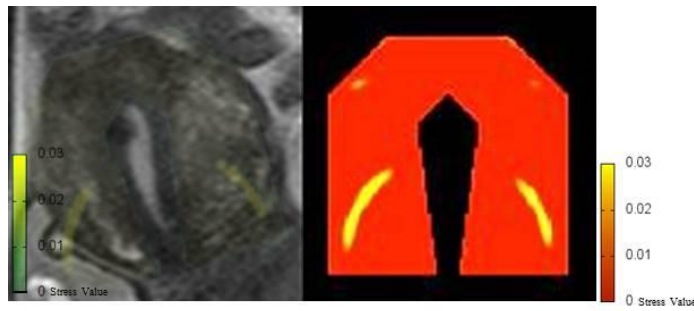

Figure A-2 Comparing MRI and simulation (5/90) [20].
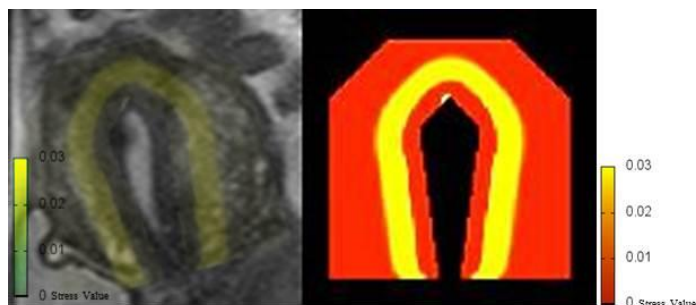
Figure A-3 Comparing MRI and simulation (10/90) [20].
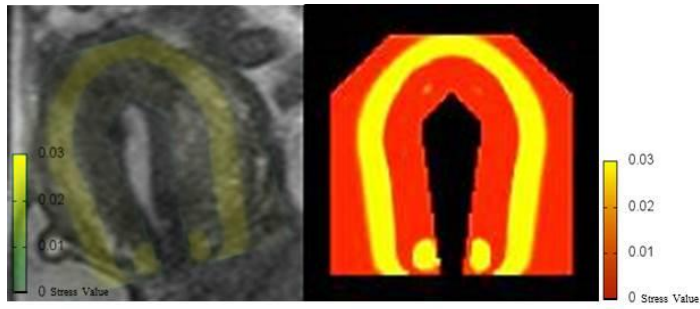
Figure A-4 Comparing MRI and simulation (15/90) [20].
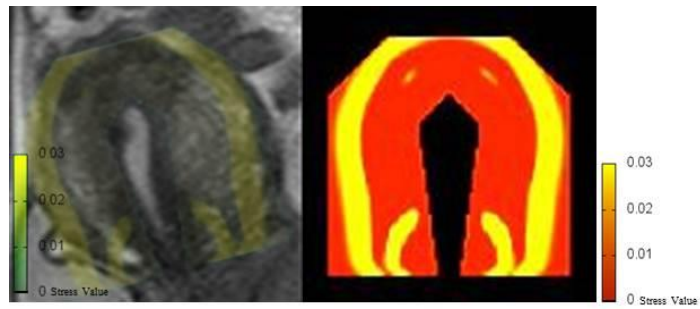
Figure A-5 Comparing MRI and simulation (20/90) [20].
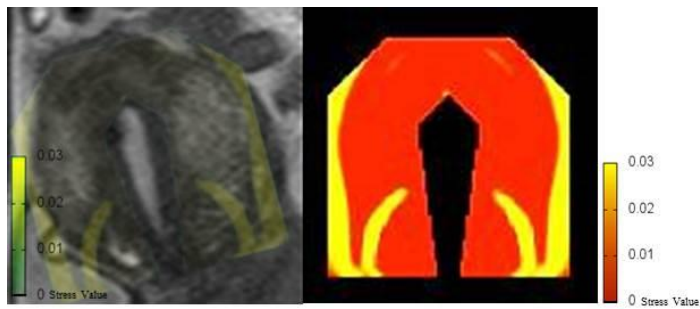
Figure A-6 Comparing MRI and simulation (25/90) [20].
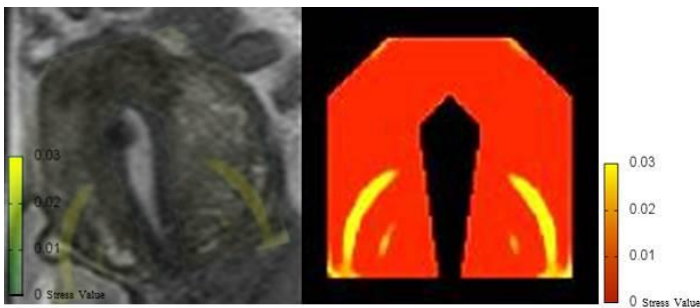
Figure A-7 Comparing MRI and simulation (30/90) [20].

Figure A-8 Comparing MRI and simulation (35/90) [20].
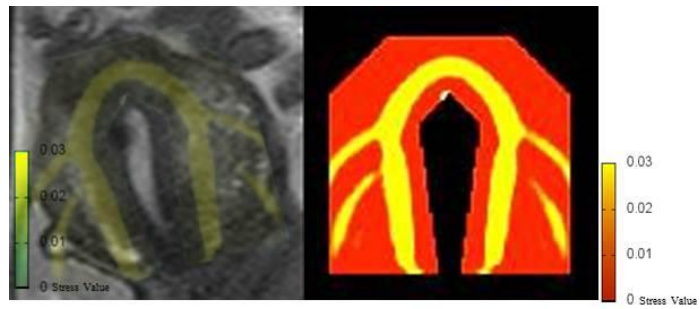
Figure A-9 Comparing MRI and simulation (40/90) [20].
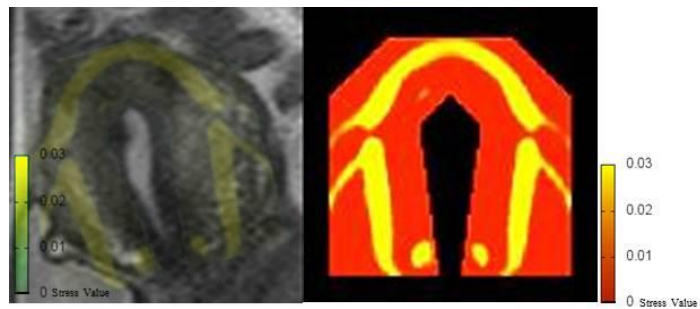
Figure A-10 Comparing MRI and simulation (45/90) [20].

Figure A-11 Comparing MRI and simulation (50/90) [20].

Figure A-12 Comparing MRI and simulation (55/90) [20].

Figure A-13 Comparing MRI and simulation (60/90) [20].

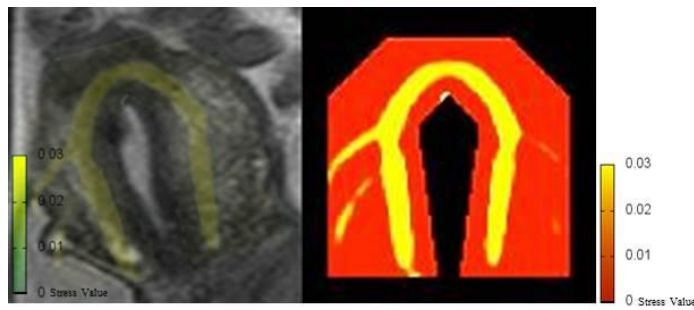Figure A-14 Comparing MRI and simulation (65/90) [20].

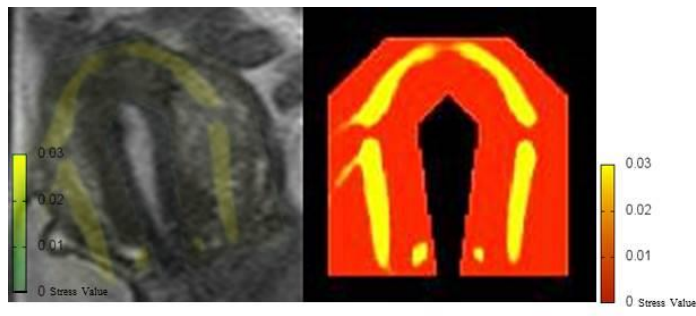Figure A-15 Comparing MRI and simulation (70/90) [20].

Figure A-16 Comparing MRI and simulation (75/90) [20].
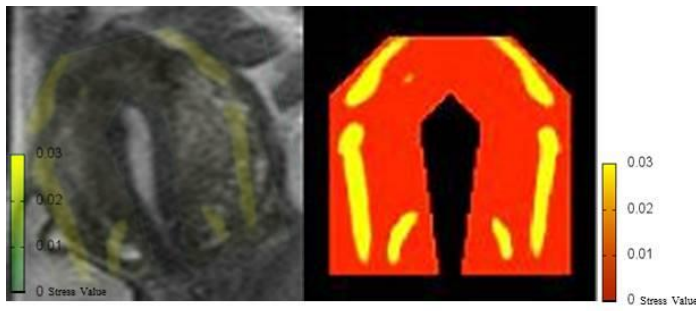

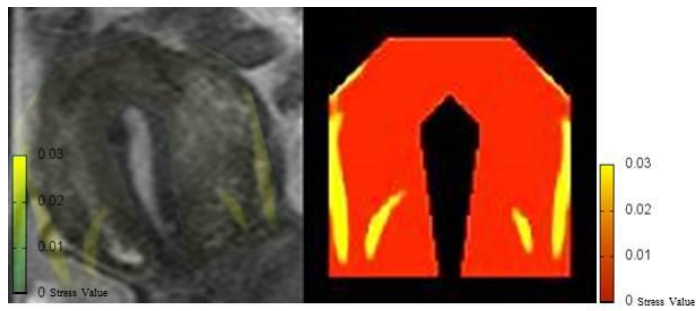Figure A-17 Comparing MRI and simulation (80/90) [20].

Figure A-18 Comparing MRI and simulation (85/90) [20].

List of Publications by the Author

Journals

1. Kentaro Mori, Yoshimitsu Tokunaga, Tetsurou Sakumoto, Akira Nakashima, Isamu Komesu, Yutaka Hata, "A Uterine Motion Classification in MRI data for Female Infertility", Bentham science, Current Medical Imaging, Volume 16, Issue 5, 2020, pp. 479 – 490.
2. Kentaro Mori, Kotaro Kitaya, Tomomoto Ishikawa, and Yutaka Hata, "A Pregnancy Prediction System based on Uterine Peristalsis from Ultrasonic Images", Intelligent Automation and Soft Computing Journal. [in press]
3. Kentaro Mori, Hiroshi Nakajima, and Yutaka Hata, "Automated Worker Skill Evaluation for Improving Productivity Based on Labeled LDA", International Journal of Machine Learning and Cybernetics, Published online: 11 November 2020.

International Conferences

4. Kentaro Mori, Atsushi Yukawa, Atsushi Kono and Yutaka Hata, "Heart Failure Diagnosis for Tagged Magnetic Resonance Images", International Conference on Machine Learning and Cybernetics (ICMLC 2017), Ningbo, China, July, 2017.
5. Kentaro Mori, Kotaro Kitaya, Tomomoto Ishikawa and Yutaka Hata, "Analysis of Endometrium Form by Using LBP for Female Infertility", International Conference on Machine Learning and Cybernetics (ICMLC 2018), Chengdu, China, July, 2018.
6. Kentaro Mori, Hiroshi Nakajima, Yasuyo Kotake, Danni Wang and Yutaka Hata, "A Relationship Between Product Quality and Body Information of Worker and its Application to Improvement of Productivity", IEEE International Conference on Systems, Man, and Cybernetics (IEEE SMC 2018), Miyazaki, Japan, October, 2018.
7. Kentaro Mori, Hiroshi Nakajima, Yasuyo Kotake, Danni Wang and Yutaka Hata, "Automated Analyzing System for Recognizing the Elemental Processes Based on the Labeled LDA", International Conference on Machine Learning and Cybernetics (ICMLC 2019), Kobe, Japan, July, 2019.
8. Kentaro Mori, Hiroshi Nakajima, Yasuyo Kotake, Danni Wang and Yutaka Hata, "Automated Worker's Skill Evaluation System Based on the Time Series Elemental Processes for Improving Productivity", IEEE International Conference on Systems, Man, and Cybernetics (IEEE SMC 2019), Bari, Italy, October, 2019.

Domestic Conferences

9. 森健太郎，徳永義光，佐久本哲郎，中島章，畑豊，"女性不妊症のための子宮動作分類 -FDTD 法を用いた可視化シミュレーションによる評価-"，第 30 回多値論理とその応用研究会，2，金沢，1 月，2017.

10. 森健太郎，徳永義光，佐久本哲郎，中島章，米須勇，畑豊，"女性不妊症を対象とした子宮運動の動作分類"，第 61 回システム制御情報学会研究発表講演（SCI' 17），345-3，京都，5 月，2017.

11. 森健太郎，徳永義光，佐久本哲郎，中島章，米須勇，畑豊，"MRI 画像に基づく女性不妊症診断支援システムの開発〜 子宮運動のクラスタリングと可視化シミュレーションによる評価〜"，兵庫県立大学　知の交流シンポジウム 2017，52，兵庫，9 月，2017

12. 森健太郎，湯河惇，河野淳，畑豊，"タグ交点の自動追跡によるファジィ推論を用いた心不全評価"，バイオメディカル・ファジィ・システム学会第 30 回年次大会（BMFSA 2017），BMFSA2017-67，大阪，11 月，2017

13. 森健太郎，北宅弘太郎，石川智基，畑豊，"超音波画像における子宮運動方向の画像解析と妊娠の評価"，2019 年電子情報通信学会総合大会，東京，3 月，2019.

14. 森健太郎，樫脇陸，松林秀彦，石川智基，畑豊，"卵巣超音波画像における空胞自動識別のための特徴量解析"，第 18 回情報科学技術フォーラム，岡山，9 月，2019.

15. 森健太郎，河野淳，畑豊，"仮想データ生成による医療診断支援システムの改善"，第 42 回多値論理フォーラム，宮崎，9 月，2019.

Other

16. "可視化シミュレーションを用いた子宮の蠕動運動解析"，Focus 事例集（第 10 号，2020 年 4 月 1 日），pp. 4-5，2020.

Award

17. 兵庫県立大学知の交流シンポジウム 2017 優秀ポスター賞，2017 年 9 月